

University of Nebraska - Lincoln
DigitalCommons@University of Nebraska - Lincoln

USGS Staff -- Published Research

US Geological Survey

2017

Camera system considerations for geomorphic applications of SfM photogrammetry

Adam R. Mosbrucker

US Geological Survey, amosbrucker@usgs.gov

Jon J. Major

US Geological Survey


Kurt R. Spicer

US Geological Survey

John Pitlick

University of Colorado

Follow this and additional works at: <http://digitalcommons.unl.edu/usgsstaffpub>

 Part of the [Geology Commons](#), [Oceanography and Atmospheric Sciences and Meteorology Commons](#), [Other Earth Sciences Commons](#), and the [Other Environmental Sciences Commons](#)

Mosbrucker, Adam R.; Major, Jon J.; Spicer, Kurt R.; and Pitlick, John, "Camera system considerations for geomorphic applications of SfM photogrammetry" (2017). *USGS Staff -- Published Research*. 1007.
<http://digitalcommons.unl.edu/usgsstaffpub/1007>

This Article is brought to you for free and open access by the US Geological Survey at DigitalCommons@University of Nebraska - Lincoln. It has been accepted for inclusion in USGS Staff -- Published Research by an authorized administrator of DigitalCommons@University of Nebraska - Lincoln.

Camera system considerations for geomorphic applications of SfM photogrammetry

Adam R. Mosbrucker,^{1*} Jon J. Major,¹ Kurt R. Spicer¹ and John Pitlick²

¹ US Geological Survey, Vancouver, WA USA

² Geography Department, University of Colorado, Boulder, CO USA

Received 17 October 2014; Revised 11 October 2016; Accepted 12 October 2016

*Correspondence to: Adam R. Mosbrucker, US Geological Survey, Cascades Volcano Observatory, 1300 SE Cardinal Court, Bldg 10, Suite 100, Vancouver, WA 98683, USA. E-mail: amosbrucker@usgs.gov

ESPL

Earth Surface Processes and Landforms

ABSTRACT: The availability of high-resolution, multi-temporal, remotely sensed topographic data is revolutionizing geomorphic analysis. Three-dimensional topographic point measurements acquired from structure-from-motion (SfM) photogrammetry have been shown to be highly accurate and cost-effective compared to laser-based alternatives in some environments. Use of consumer-grade digital cameras to generate terrain models and derivatives is becoming prevalent within the geomorphic community despite the details of these instruments being largely overlooked in current SfM literature.

A practical discussion of camera system selection, configuration, and image acquisition is presented. The hypothesis that optimizing source imagery can increase digital terrain model (DTM) accuracy is tested by evaluating accuracies of four SfM datasets conducted over multiple years of a gravel bed river floodplain using independent ground check points with the purpose of comparing morphological sediment budgets computed from SfM- and LiDAR-derived DTMs. Case study results are compared to existing SfM validation studies in an attempt to deconstruct the principle components of an SfM error budget.

Greater information capacity of source imagery was found to increase pixel matching quality, which produced eight times greater point density and six times greater accuracy. When propagated through volumetric change analysis, individual DTM accuracy (6–37 cm) was sufficient to detect moderate geomorphic change (order 100 000 m³) on an unvegetated fluvial surface; change detection determined from repeat LiDAR and SfM surveys differed by about 10%. Simple camera selection criteria increased accuracy by 64%; configuration settings or image post-processing techniques increased point density by 5–25% and decreased processing time by 10–30%.

Regression analysis of 67 reviewed datasets revealed that the best explanatory variable to predict accuracy of SfM data is photographic scale. Despite the prevalent use of object distance ratios to describe scale, nominal ground sample distance is shown to be a superior metric, explaining 68% of the variability in mean absolute vertical error. Published 2016. **This article is a U.S. Government work and is in the public domain in the USA**

KEYWORDS: Structure-from-Motion photogrammetry; camera system configuration; high-resolution remote sensing; topographic data accuracy; LiDAR

Introduction

Three-dimensional (3D) digital terrain models (DTMs) have become a staple in geosciences for characterizing topographic surfaces and especially for analyzing spatial and temporal geomorphic change in many environments. Various remote sensing methods are used to obtain topographic point measurements, including traditional photogrammetry (e.g. Walker and Petrie, 1996), airborne laser scanning (ALS) and terrestrial laser scanning (TLS) (light detection and ranging [LiDAR] collectively; e.g. Heritage and Hetherington, 2007; Anderson and Pitlick, 2014), and more recently digital imagery that feeds structure-from-motion (SfM) photogrammetry (e.g. James and Robson, 2012). As SfM becomes more widely applied to process-oriented research and for analysis of geomorphic change detection, it becomes imperative to understand its utility, limitations, and particularly the accuracy of DTMs derived from these data. Several studies have shown that

SfM can generate highly-accurate and high-resolution DTMs more efficiently and cost-effective than laser-based alternatives in suitable environments (Niethammer *et al.*, 2010; James and Robson, 2012; Nouwakpo *et al.*, 2016). Accuracy of SfM-derived data has been evaluated previously by comparing results to data derived from traditional photogrammetry (James and Robson, 2012; Rosnell and Honkavaara, 2012; Welty *et al.*, 2013), ALS (Fonstad *et al.*, 2013; Dietrich, 2016), TLS (Castillo *et al.*, 2012; James and Robson, 2012; Westoby *et al.*, 2012; James and Quinton, 2014; Gómez-Gutiérrez *et al.*, 2014; Thoeni *et al.*, 2014; Micheletti *et al.*, 2015b; Nouwakpo *et al.*, 2016; Smith and Vericat, 2015), and terrestrial topographic surveys (Fonstad *et al.*, 2013; Javernick *et al.*, 2014; Woodget *et al.*, 2015; Smith and Vericat, 2015). These comparisons promote the utility of SfM, which is rapidly becoming part of the geomorphologist's toolbox (Gomez, 2014).

A basic principle of geomatics, and photogrammetry in particular, is that accuracy is related to photographic scale, commonly

described as the ratio between distance in a photograph and its corresponding 'real world' distance (e.g. the representative fraction for a 30-m-wide river represented as a 1-cm-wide object in a photograph is 1:3000 scale). Consumer-grade digital cameras are regularly used to acquire SfM source imagery from a variety of platforms at different scales. For a given camera system, scale can be changed by increasing or decreasing object distance (e.g. the distance, or range, between the camera and ground surface). Several studies have reported ratios of precision and accuracy of SfM data to object distance on the order of 1:1000 (James and Robson, 2012; Micheletti *et al.*, 2015a; Smith and Vericat, 2015). However, due to the lack of standardized camera systems used in these studies, photographic scale is determined by more than object distance alone.

Additionally, digital cameras are relatively easy to use; careful selection and configuration of these instruments has largely been overlooked in current SfM literature within the geoscience community. Two recent reviews, Smith *et al.* (2016) and Eltner *et al.* (2016), synthesize current best practices and discuss error sources regarding SfM workflows, but do not provide in-depth camera system considerations.

In the present contribution, we hypothesize that optimizing imagery acquired for SfM photogrammetric applications in geomorphology can increase DTM accuracy. First, we provide a review and practical discussion of quantitative image quality with regard to camera system selection and configuration. Next, we test our hypothesis by evaluating the accuracy of SfM surveys conducted over multiple years of a gravel bed river floodplain, using independent ground check points with the purpose of comparing morphological sediment budgets computed from SfM- and LiDAR-derived DTMs (a common yet restrictive application). Lastly, we compare our findings to other studies and begin to deconstruct the principle components of a SfM error budget, with specific consideration of point density and scale.

Review of SfM photogrammetry

Mathews *et al.* (2006) described photogrammetry as 'the art and science of making measurements from photographs'. Photogrammetric methods produce 3D point measurements from photographs, where objects or surfaces are captured from multiple perspectives. Images need to have a high degree of overlap because the principle of stereoscopic parallax is used to solve collinearity equations to determine the position of 3D objects projected onto a two-dimensional (2D) image plane (e.g. Mathews, 2008). Traditional photogrammetry often utilizes aerial photographs acquired with calibrated (metric) large-format (i.e. >12 900 mm² film frame) camera systems at near nadir angle of view (e.g. Walker and Petrie, 1996).

Traditional photogrammetry relies on identification of ground control points (GCPs) having known geodetic (i.e. geographic or real-world) coordinates to calibrate camera parameters and solve collinearity equations (e.g. Buckley *et al.*, 2004; Fonstad *et al.*, 2013). Close-range oblique photogrammetry using non-calibrated (non-metric), small-format (<900 mm² sensor), and consumer-grade digital camera systems has become common in the past decade (e.g. Sturznegger and Stead, 2009; Mosbrucker, 2010; Diefenbach *et al.*, 2012; Rosnell and Honkavaara, 2012). Like traditional photogrammetry, the close-range oblique photogrammetry method requires robust camera-calibration techniques and GCPs to solve collinearity equations and orient the photogrammetric model (Chandler, 1999; Mathews *et al.*, 2006).

In contrast to traditional and close-range oblique photogrammetry, SfM relaxes some of these constraints, making image

acquisition and processing significantly faster and easier for those not subject-matter experts (Castillo *et al.*, 2012; James and Robson, 2012; Woodget *et al.*, 2015; Gomez *et al.*, 2015). Initially an open-source product of 3D computer vision (Ullman, 1979), SfM leverages parallel processing architecture and automated pixel-matching algorithms based on luminance and color gradients. Robust image matching and multi-view stereo (MVS) algorithms are better suited for reconstruction of dense 3D point clouds from large sets of un-sorted oblique photographs (where radiometric variation and scale changes throughout a single frame). For this reason, SfM is often referred to as 'SfM-MVS' to describe the combined workflow (e.g. James and Robson, 2012). In contrast, traditional and close-range oblique photogrammetric workflows employ kernel-based cross-correlation techniques to one image pair at a time and require minimal changes to photographic scale (e.g. Gruen, 2012). SfM algorithms solve collinearity equations prior to scaling and transforming a photogrammetric model into a geodetic reference system using a minimum of three GCPs and/or camera positions (e.g. Rippen *et al.*, 2015; Smith *et al.*, 2016). Very large numbers (>100 000) of auto-identified tie-points, rather than a few GCPs, determine camera calibration parameters. Therefore, accuracy of traditional photogrammetric data depends heavily on GCP quality, whereas SfM accuracy is affected more by image characteristics.

Much of the SfM workflow is automated, and software (including open source and freeware) is widely available. A few software packages integrate SfM algorithms for initial scene reconstruction with traditional photogrammetric methods to optimize camera calibration parameters using GCPs (e.g. Agisoft Photoscan). More comprehensive discussions of SfM techniques and workflows are presented in Snavely *et al.* (2008), James and Robson (2012), Westoby *et al.* (2012), Fonstad *et al.* (2013), Javernick *et al.* (2014), Smith *et al.* (2016), and Eltner *et al.* (2016).

Image Optimization

Photogrammetric applications are like any other form of surveying – mastery of the instrumentation is required to achieve the best results. For SfM surveys employing consumer-grade digital cameras, many techniques can be drawn from landscape photographic principles, which seek to maximize image quality for dramatic enlargement. The following discussion reviews camera system fundamentals and provides practical guidelines on the use of these instruments to maximize the information capacity of SfM datasets for geomorphic applications. Information capacity of each image, and the dataset as whole, is improved by careful camera system selection, configuration, and image acquisition.

A key constraint to SfM camera calibration, point density, and DTM accuracy is pixel-level feature detection within source imagery. Gruen (2012) states that pixel matching is the 'most important function in digital photogrammetry (and) automated modelling'. This pixel matching is a function of image quality, geometry, lighting conditions, and surface characteristics (e.g. texture). Accurate pixel matching is required for well-defined camera calibration parameters, SfM tie point generation, and subsequent MVS densification, which usually increases point density by >2 orders of magnitude (Smith *et al.*, 2016). It is important to distinguish between the accuracy of individual 3D points and subsequent point density necessary to capture an accurate surface representation within a vector- or raster-based topographic model (Chandler and Fryer, 2013). Westoby *et al.* (2012) and Gienko and Terry (2014) demonstrate that accuracy of SfM-derived

3D models is highly correlated with the number of points used to reconstruct a surface (i.e. point density).

Camera system selection

Consumer-grade digital camera systems include small-format compact cameras, interchangeable lens mirrorless, and digital single-lens reflex (DSLR). Medium-format (e.g. 1400 mm² sensor) systems are larger and prohibitively expensive for many projects (\geq US\$14 000). Recently, geomorphic studies have been conducted with a variety of camera systems, from a smart phone to a DSLR. Micheletti *et al.* (2015b) produced DTMs with centimeter-level precision using smart phone imagery at close range (\leq 10 m) and a fully automated web-based analytical service. However, their accuracy improved significantly with the use of a DSLR and commercial close-range photogrammetry software. Thoeni *et al.* (2014) compared five cameras (16–330 mm² sensors) to a TLS benchmark at close range (<10 m) and found a general improvement in camera system quality correlated with decreasing GCP residuals. But how can imagery from a variety of camera systems be quantified and optimized for SfM applications? Several fundamental photographic concepts must be explained before discussing practical guidelines related to each. A summary of these, and additional, guidelines is provided in the Discussion section.

A digital camera is comprised of three subsystems: a lens, sensor, and processor. Ideally, these provide imagery which has high effective resolution (lens and sensor), high dynamic range (sensor and processor), high signal-to-noise ratio (SNR) (sensor and processor), and low distortion (lens) (Cao *et al.*, 2010). For photogrammetric surveying, camera selection criteria should focus on maximizing information capacity of each image dataset, which Cao *et al.* (2010) found to be the product of resolution and dynamic range. Most of the following criteria can be found in technical specifications supplied by camera manufacturers prior to purchasing.

Image resolution is described by the number of pixels (megapixels; MP) a sensor records to an image file. However, a more useful metric is effective resolution, a consequence of detail lost through a sensor's color filter array and lens, which can only be determined by testing the camera system in a laboratory environment; laboratory results for many camera-lens combinations can be found on the web. A Bayer color filter array is the most common type, while other proprietary alternatives (e.g. Fuji X-Trans or Sigma Foveon) can produce

greater effective resolution for a given number of pixels (Cramer, 2004). Bayer demosaicing typically requires the use of an anti-aliasing filter to blur details finer than the resolution of the sensor to prevent unwanted artifacts, but options that 'cancel out' the anti-aliasing filter are increasingly available. SfM practitioners should select a camera system with high effective resolution (\geq 16 MP) that has no anti-aliasing filter effects.

Dynamic range, commonly described by a base-2 logarithm called exposure value (EV), is a function of the bit depth of a sensor's analogue-to-digital converter (ADC), SNR, color sensitivity, transmission, and vignetting (Cao *et al.*, 2010). For example, a 12-bit ADC has 12 EVs of dynamic range (if linear). Ideally, dynamic range should be sufficient enough to capture the entire range of luminance within a scene (i.e. pixel information in both bright and dark areas). The best consumer-grade digital cameras utilize sensors with \geq 14-bit non-linear ADCs.

Despite sophisticated reduction algorithms, digital noise can significantly degrade image quality, especially in low ambient lighting conditions. Comparable to film grain for an analogue camera, this noise is expressed as SNR and normalized ISO values (Cramer, 2004). SNR describes how well the signal (i.e. light) is distinguished from background noise. ISO describes a sensor's absolute sensitivity to light. For example, changing a camera's ISO setting from 100 to 200 (or 1 EV) requires half as much light to achieve the same exposure; however, this signal amplification also amplifies noise in cameras not ISO-invariant. Noise is caused by random distribution of photons and sensor temperature; long exposure times can overheat a sensor. Cao *et al.* (2010) found noise to be primarily dependent on physical sensor size; larger sensors can have greater pixel spacing (and thus fewer photon interactions) along with reduced thermal energy. Users should choose a camera with a sensor size \geq 300 mm² or one that has been found to be ISO-invariant.

Another constraint to SfM accuracy is radial distortion and associated calibration of the camera lens (Rosnell and Honkavaara, 2012; Sanz-Ablanedo *et al.*, 2012). This distortion is highly correlated to lens focal length, which determines a camera system's field of view. Focal length is defined by its optical construction, but the field of view can change if a lens is mounted to a camera with a different sensor size (Figure 1a). For consumer-grade digital cameras, a focal length multiplier is used to relate sensor size to the field of view from a full-frame (or FX-size) camera which has a \sim 864 mm² sensor (the same

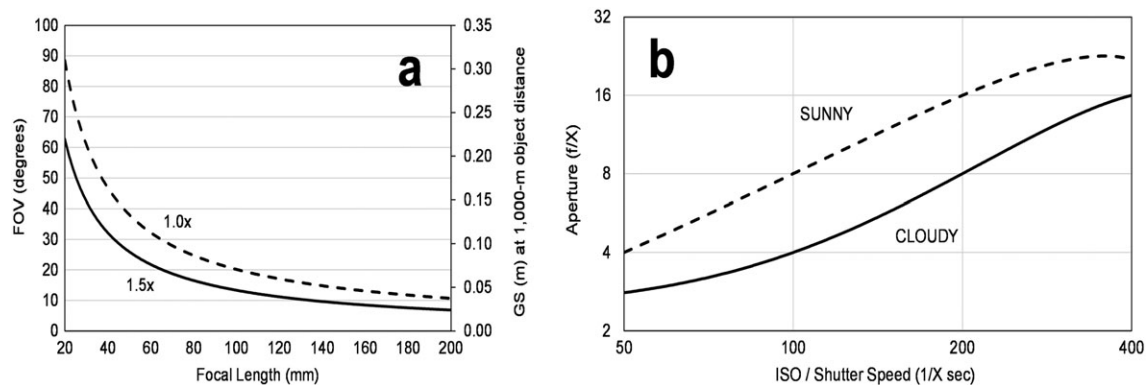


Figure 1. Interaction between several camera system parameters. Sensor size (a) influences horizontal field of view (FOV), and thus nominal ground sample (GS) distance for a given focal length at a constant object distance (1000 m); both sensors have the same resolution (24 MP) so the effect is caused by pixel size differences (1.0 \times focal length multiplier for the full-frame, or FX, Nikon D610 with 6.0 μ m pixels; 1.5 \times focal length multiplier for the APS-C Nikon D7200 with 3.9 μ m pixels). Known by photographers as the 'sunny-16 rule', this exposure rule-of-thumb (b) generalizes the relationship between aperture, ISO, and shutter speed for two ambient lighting conditions (sunny and cloudy); At a given aperture, shutter speed is the reciprocal of ISO along the line (e.g. proper exposure on a sunny day is approximately f/8 at 1/100 s at ISO 100).

dimensions as an analogue 35-mm film frame). For instance, a lens with a focal length of 20 mm mounted on a full-frame camera has a field of view that is 90-m wide at a distance 50 m from the object. If the same lens is mounted to a smaller sensor (e.g. $>300\text{mm}^2$ or APS-C size) with a focal length multiplier of 1.5, the equivalent focal length is 30 mm, corresponding to a 60-m-wide field of view (a 30% increase in scale). Most digital cameras have a focal length multiplier between 1.3 and 2.0. While the use of small focal lengths (or wide-angle) is common to provide the largest field of view (e.g. Eltner *et al.*, 2016), these are subject to increased radial distortion and smaller scale for a given object distance, which can degrade accuracy. These effects are intensified for ultra-wide-angle (fish-eye) lenses ($\sim 120^\circ$ – 220° horizontal field of view) popular among many ‘action cameras’ (e.g. GoPro products) so are best avoided. For sensors with 1.0–2.0 focal length multipliers, quality fixed focal length lenses (i.e. non-variable or zoom) from 35 to 105 mm generally produce the least distortion and greatest effective resolution, which is still often 30–50% less than a sensor’s native resolution. Lens-related resolution losses are caused by optical blur, chromatic aberrations, and distortion.

The stability of a camera system’s internal geometry, a source of error, can be improved by using a rigid metal camera body with a stable and fixed lens (i.e. non-zoom and non-retractable) (Shortis *et al.*, 2006; Niethammer *et al.*, 2010; Rosnell and Honkavaara, 2012). Even a small change in focus distance, which physically changes the optical configuration, should be minimized for high-accuracy work; it is common practice to tape the lens focus ring (at an appropriate distance for optimal depth-of-field) to ensure stability of the internal camera calibration (e.g. Chandler *et al.*, 2007; Diefenbach *et al.*, 2012; Nouwakpo *et al.*, 2016). For geomorphic work, focus is often set at infinite distance (e.g. Sanz-Ablanedo *et al.*, 2012), though it is becoming increasingly difficult to find autofocus lenses that have a mechanical stop at infinity. Thankfully, many of the highest-quality DSLR lenses available are manual focus only with precise stops at infinity.

The most common type of camera for SfM image acquisition, interchangeable-lens DSLRs, do not always provide the greatest image quality. In recent years, non-interchangeable fixed-lens compact cameras have become available featuring large sensors, high-quality optics, and sophisticated processors; because engineers can optimize the optical formula and lens placement, these cameras often produce images with greater effective resolution and equivalent dynamic range as their larger counterparts. Additionally, the relatively small payload of these cameras makes them increasingly deployable via unmanned aircraft systems (e.g. Lisein *et al.*, 2013). Lower-quality compact camera systems can produce acceptable results in optimal lighting conditions at short ($\sim 10\text{m}$) object distances (Micheletti *et al.*, 2015a; Thoeni *et al.*, 2014), but as object distance increases and/or ambient lighting conditions worsen (e.g. requiring greater dynamic range), users should prioritize GCP quality to support an optimization routine (e.g. available in Photoscan) or consider using a higher quality camera system.

Camera system characteristics should be considered when selecting a lens calibration model to use for 3D reconstruction. In addition to internal stability, radial distortion is more easily modeled in fixed focal length lenses than tangential distortion often found in zoom lenses. If a zoom lens or automatic focusing is used, it is best to treat each image as if it were from a different camera during scene reconstruction using a photo invariant calibration model (Shortis *et al.*, 2006; Rosnell and Honkavaara, 2012). However, a fixed focal length and fixed focus (i.e. using tape) lens is optimal; these

lenses allow the use of a more accurate block invariant calibration model. Digital image processing can correct the geometrical effect of aberrations and distortion (in real-time with some cameras, during post-processing, or within a SfM workflow); however, there remains a local loss of effective resolution away from the center of the frame.

Camera system configuration

Provided the camera system allows manual configuration of key parameters, as most do, a lot can be done to maximize information capacity through careful selection of camera system settings. Two key concepts should be prioritized: proper exposure and focus.

Proper exposure retains pixel information in both bright and dark areas of a scene. Exposure, or the amount of light the sensor records, is a function of lens aperture, shutter speed, and (to a lesser degree) ISO (Figure 1b). Optimizing these three components can only be done in very bright lighting conditions; an increase of 1 EV requires twice as much light reaching the sensor. The camera should be configured at the lowest ISO setting possible to mitigate noise (increase SNR) and maximize dynamic range. Shutter speed controls the duration of time the sensor is illuminated, typically described in units of fractions of a second (e.g. $1/250\text{s}$ is 1 EV less than $1/125\text{s}$). Shutter speed should be short enough to overcome camera and/or subject motion (dependent on focal length, object distance, and velocity). A longer focal length, shorter object distance, and/or greater velocity requires a faster shutter speed. A good rule-of-thumb for minimum shutter speed is the reciprocal of twice the focal length (e.g. $1/100\text{s}$ for a 50 mm focal length) for stationary platforms, or $<1/400\text{s}$ for moving platforms such as aircraft. Very high-resolution sensors ($\geq 24\text{MP}$) require faster shutter speeds to achieve the greatest effective resolution. Camera shutters can be electronic (at the sensor), or mechanical (in front of the sensor or inside the lens). Lastly, aperture refers to the opening of a diaphragm within a lens. A large aperture (small f-stop value) has a larger diameter opening than a small aperture (large f-stop value). An increase of 1 EV is achieved by opening the lens by 1 f-stop (e.g. $f/8.0$ to $f/5.6$). ISO and aperture have an inverse relationship to shutter speed; if a greater shutter speed is required, the user needs to select a larger aperture or greater ISO value to achieve the same exposure. Generally, users should select the lowest ISO value possible while maintaining acceptable shutter speed and aperture values.

Lens aperture selection affects more than exposure, causing many photographers to prioritize its setting over ISO or shutter speed. Aperture selection can affect several areas of information capacity loss, including effective resolution, vignetting (i.e. reduction of brightness in the image corners), and chromatic aberration (i.e. distortion caused by the inability to focus all wavelengths of color to the same focal plane). Lenses with apochromatic optical formulas that include low dispersion and/or aspheric glass elements are ideal to minimize information capacity loss, but aperture selection is of greater importance. The optimal aperture for any lens is typically 1–3 f-stops smaller than the maximum aperture available (e.g. selecting $f/5.6$ – 8.0 is optimal for many $f/2.0$ – 2.8 lenses). Additionally, effective resolution of small-format camera systems is limited by diffraction at apertures smaller than $\sim f/11$, creating a fairly narrow working range (2–3 EV).

For terrestrial or low-altitude aerial photogrammetric surveys, depth-of-field should be considered when selecting lens focal length, aperture, and object distance to ensure sharp focus (i.e. maximum effective resolution) throughout the scene.

When hyperfocal distance is exceeded, such as with most aerial surveys, the lens can simply be focused (and taped) at infinity and aperture set to optimal as depth-of-field is not a concern.

Other considerations include image file format and color space. RAW files (32-bit; compared to 8-bit JPEG files) preserve more dynamic range and feature less noise (Mosbrucker *et al.*, 2015a). RAW files (not available on all cameras) can be recorded prior to in-camera processing and in addition to JPEG files to use in case of over- or under-exposure, but are not currently supported by SfM software so they require conversion. In addition to the sensor's dynamic range, the color space, or coordinate system, of RGB (red–green–blue) image files determines data precision and range at the pixel level. Selecting a wide color space (e.g. AdobeRGB versus sRGB) helps improve information capacity. Experience has shown that using AdobeRGB color space (not available on all cameras) can match 5–10% more points/frame than the same RAW image files referenced to sRGB in 30% less time.

Lastly, internal stability of the camera system can be compromised by standard features and default settings included in many consumer-grade digital cameras. Users should disable features such as autofocus, optical- or sensor-based image stabilization systems, in-camera distortion correction (unless explicitly defined during reconstruction), auto image rotation, and noise reduction filters (which can smooth out fine details) (Shortis *et al.*, 2006; Sanz-Ablanedo *et al.*, 2012).

Image acquisition

Micheletti *et al.* (2015b) notes that image acquisition 'remains (a) delicate step in (an) otherwise automated' workflow. In general, image acquisition involves capturing overlapping photographs of the study area from multiple locations; all areas of interest should be in ≥ 3 photographs (James and Robson, 2012). This is typically performed by relocating one camera system to observe a static scene, but can also be accomplished using a network of stationary cameras observing a dynamic scene (e.g. James and Robson, 2014). Aerial surveys can have important advantages over ground-based image acquisition, including increased spatial coverage, reduced occlusion, and greater pixel matching reliability due to greater angle of incidence in low-relief terrain (e.g. Smith and Vericat, 2015). Regardless of the platform used (i.e. hand-held, pole-mounted, lighter-than-air blimp, kite, unmanned aerial vehicles [UAV], or manned aircraft), mission planning considerations for high-accuracy surveys include information capacity (i.e. camera system selection and configuration), lighting conditions, surface characteristics, image geometry, and image overlap.

Ambient lighting conditions can significantly alter apparent surface characteristics such as texture. While an overcast day or solar noon maximizes solar incident angle and minimizes shadows (James and Robson, 2012; Gienko and Terry, 2014; Micheletti *et al.*, 2015b), side light can enhance surface texture in some environments. Pixel matching can fail or result in reduced accuracy in areas of low contrast or noise (e.g. homogeneous surfaces or large shadows) (Niethammer *et al.*, 2012; Rosnell and Honkavaara, 2012; Chandler and Fryer, 2013; Gomez *et al.*, 2015; Micheletti *et al.*, 2015b). While these conditions should be avoided if possible, imagery can be optimized to mitigate scenes with dynamic range larger than a given sensor can record to one file. Dynamic range in SfM photogrammetry has been discussed in Rosnell and Honkavaara (2012) and analyzed by Guidi *et al.* (2014); their experiment showed how digitally pre-processing three 14-bit images into a single tone-mapped 8-bit high dynamic

range (HDR) image using Photoshop improved feature matching by 5–13% (some cameras now offer in-camera HDR processing at time of capture). The greatest improvement for geomorphologic applications is likely realized in scenes that include reflective water or snow and dark shadows. Similarly, Gienko and Terry (2014) suggest using polarizing filters to suppress reflections and glare in imagery. Guidi *et al.* (2014) found that optical pre-processing of imagery with a polarizing filter can produce 5–25% more matched points, depending on scene characteristics.

In all types of photogrammetry, large-scale imagery commonly produces greater accuracy and precision due to its ability to resolve small features (e.g. Buckley *et al.*, 2004; Micheletti *et al.*, 2015b). Nominal ground sample (GS) distance is a convenient way to describe scale when comparing different DTM source imagery. For digital photogrammetry, GS distance is the spatial resolution of the imagery – the distance on the ground represented by the edge of an individual pixel in an image file – which changes across the frame of oblique image. GS distance is computed from camera sensor dimensions, lens focal length, and object distance (Figure 1a). In general, the range of typical GS distance for the most common camera systems can be computed using simple dimensional analysis; a 24-MP sensor with a 370–860-mm² sensor at a 1000-m object distance produces a GS distance of 2–30 cm if the focal length is 20–200 mm, respectively (Figure 1a). For close-range surveys (e.g. 10-m object distance), this GS distance range scales down to 0.02–0.30 cm.

For SfM photogrammetry, several studies have found that optimal results are achieved by acquiring imagery at multiple scales – the entire study area supplemented by detailed imagery at greater scale (Gienko and Terry, 2014; Chandler and Fryer, 2013; Micheletti *et al.*, 2015a, 2015b). This is best accomplished by changing object distance (or altitude for aerial surveys) to maintain a stable camera for block invariant calibration. There is an inverse relationship between GS distance and the minimum number of images required to adequately cover the spatial extent and topographic complexity (i.e. avoid occlusions); smaller GS distance values require a greater number of images and computational abilities (James and Robson, 2012; Smith *et al.*, 2016).

Weak image block geometry can lower point density and cause small-magnitude (order ≤ 0.2 m) dome-like deformations (i.e. a bulge in center of surface model) which affect the spatial distribution of errors within SfM-derived DTMs (James and Robson, 2014; Javernick *et al.*, 2014; Nouwakpo *et al.*, 2016; Woodget *et al.*, 2015). This deformation, attributed to linear and near-parallel image blocks, is avoided in traditional photogrammetric workflows by judicious use of GCPs. James and Robson (2012) found that additional GCPs can reduce error in the final georeferenced DTM but a diminishing return is experienced due to the rigid transformations typically used, which prevent an optimal fit to control points. Instead, this is mitigated in SfM by emphasizing GCP quality over quantity (James and Robson, 2012; Javernick *et al.*, 2014) and strengthening the image block with oblique and convergent imagery captured at multiple scales (Wackrow and Chandler, 2008, 2011; Chandler and Fryer, 2013; James and Robson, 2014). The most robust geometric solutions are from converging optical axis at $< 20^\circ$ (Gienko and Terry, 2014), $\geq 80\%$ image overlap, and an angle of incidence $\geq 40^\circ$ (which may require an elevated or airborne platform; Smith and Vericat, 2015). Lastly, in the absence of available GCPs, datasets can be aligned relative to each other by applying an iterative closest point (ICP) algorithm (e.g. James and Robson, 2012; Micheletti *et al.*, 2015a) to optimize the transformation between two point clouds over stable areas.

Case Study

We use an opportunistic case study conducted on a gravel bed river floodplain, an ideal environment for SfM application, to illustrate the relationship between image optimization and DTM accuracy. We first conduct an independent comparison between TLS- and SfM-derived DTMs. We then use ground check points to determine the absolute accuracy of each DTM, and propagate these individual errors to DTMs of difference (DoD) comparing each method to a previously acquired DTM derived from airborne LiDAR. Geomorphic change detection using DoDs is one of the most restrictive morphometric analyses commonly performed using topographic data, requiring robust geodetic control and minimization of systematic errors. Absolute accuracy describes the consistency of a DTM with external data sources (geographic reference frame required), while relative accuracy describes the internal consistency of a DTM (with its own GCPs).

Study site

The May 18, 1980, eruption of Mount St Helens, Washington, consisted of a 2.5 km³ debris avalanche followed by a blast density current, pyroclastic flows, lahars, and tephra falls (e.g. Lipman and Mullineaux, 1981). These disturbances severely altered the hydrogeomorphic regime of the upper North Fork Toutle River, whose 450 km² basin includes the north flank of the volcano. More than three decades after the eruption, the river continues to transport an average of three million tonnes (Mg) of suspended-sediment per year; daily average concentration is 30–80 000 mg/L (Mosbrucker *et al.*, 2015a).

Our study area is a 500-m-long reach of the upper North Fork Toutle River (46°16'24"N 122°15'33"W). It occupies 105 000 m² of the debris avalanche surface (Figure 2). The active river channel through the reach is about 10 m wide and <1 m deep and it frequently changes position across the floodplain. The reach features 10–30-m-tall near-vertical banks separated by a 170-m-wide floodplain (Figure 3). The reach is ideal for successful use of SfM; it provides an appropriate analysis extent, relatively rapid geomorphic change of sufficient magnitude to exceed measurement error, highly textured surfaces, and is sparsely vegetated, which precludes the need for point-filtering algorithms to model the bare-earth surface (James *et al.*, 2012; Woodget *et al.*, 2015; Staines *et al.*, 2015).

Field data collection methods

Ground surveys

Precision ground-based surveying is commonly used to establish geodetic control, provide GCPs (model generation), and ground check points (model evaluation) for remote sensing of large areas. In order to independently assess accuracies of TLS- and SfM-derived DTMs, we surveyed nearly 1200 ground check points, referenced to an absolute coordinate system and datum (Figure 2b). Immediately following the 1980 eruption of Mount St Helens, the United States Geological Survey (USGS) established a network of stream channel cross-sections that have been surveyed repeatedly (Mosbrucker *et al.*, 2015b). One of these cross sections intersected the study reach. Short segments of a longitudinal profile along the active edge of water or channel thalweg were commonly surveyed on the same date as a cross-section. Surveys conducted in 2010–2014 used a reflectorless total station (Topcon GPT-7500; 1 arcsecond angle resolution) and real-time-kinematic global navigation satellite system (RTK-GNSS) instruments (Trimble R7/R8) using methods described in Rydlund and Densmore (2012) and Mosbrucker *et al.* (2015b). The overall mean accuracy (weighted by number of points) of these check points was 8 cm horizontal (XY) and 11 cm vertical (Z). More than 60% of the points had an absolute vertical accuracy <10 cm.

Terrestrial laser scanning (TLS) surveys

For more than a decade, a common method for obtaining topographic data within the geosciences has been airborne laser scanning, or LiDAR, which is touted for its high-resolution, precision, ability to efficiently cover broad swaths of terrain, and ability to obtain measurements beneath moderate vegetation cover (Glennie *et al.*, 2013; Passalacqua *et al.*, 2015). Most airborne systems use an aircraft-mounted near-infrared laser to measure the distance to and reflectance of objects or surfaces. Geodetic coordinates for laser-point positions are computed from continuous onboard GNSS and inertial measurement unit solutions corrected to ground station positions. More recently, TLS has become a viable option to obtain high-resolution measurements of topography within relatively small areas (e.g. Bangen *et al.*, 2014). A TLS system consists of a hand-held (e.g. James and Quinton, 2014) or tripod-mounted (e.g. Heritage and Hetherington, 2007) scanner that uses a similar laser-ranging technique as airborne systems. In the case of a tripod-mounted scanner, the instrument rotates

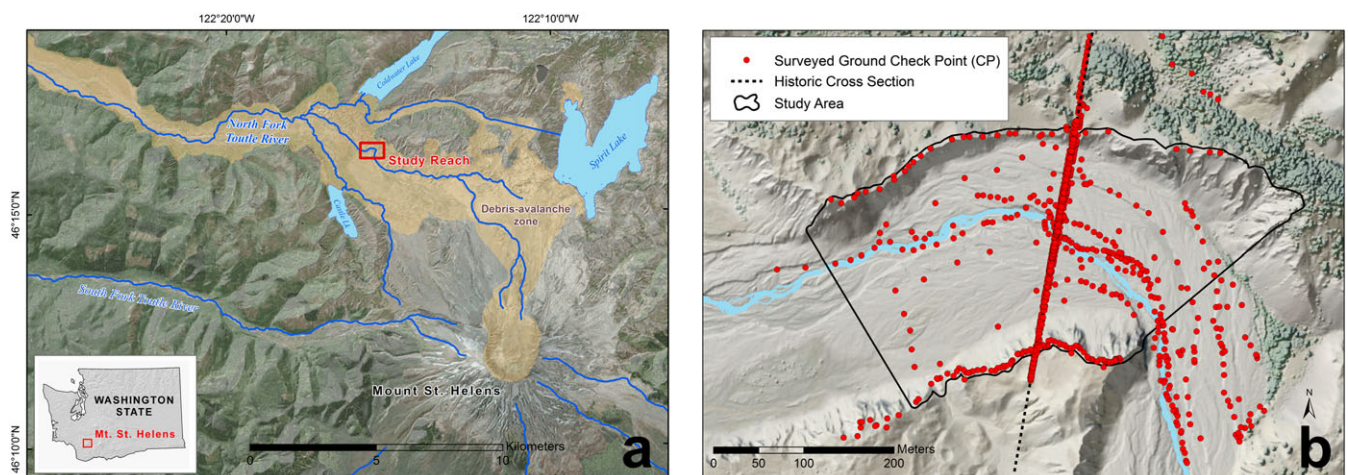


Figure 2. Location map of study reach (a) along North Fork Toutle River downstream of Mount St Helens in Washington State and detailed location map (b) of surveyed ground check points (CPs) in study reach. Ground CP density is very high along historic stream channel cross-section line in the center of the map. [Colour figure can be viewed at wileyonlinelibrary.com]

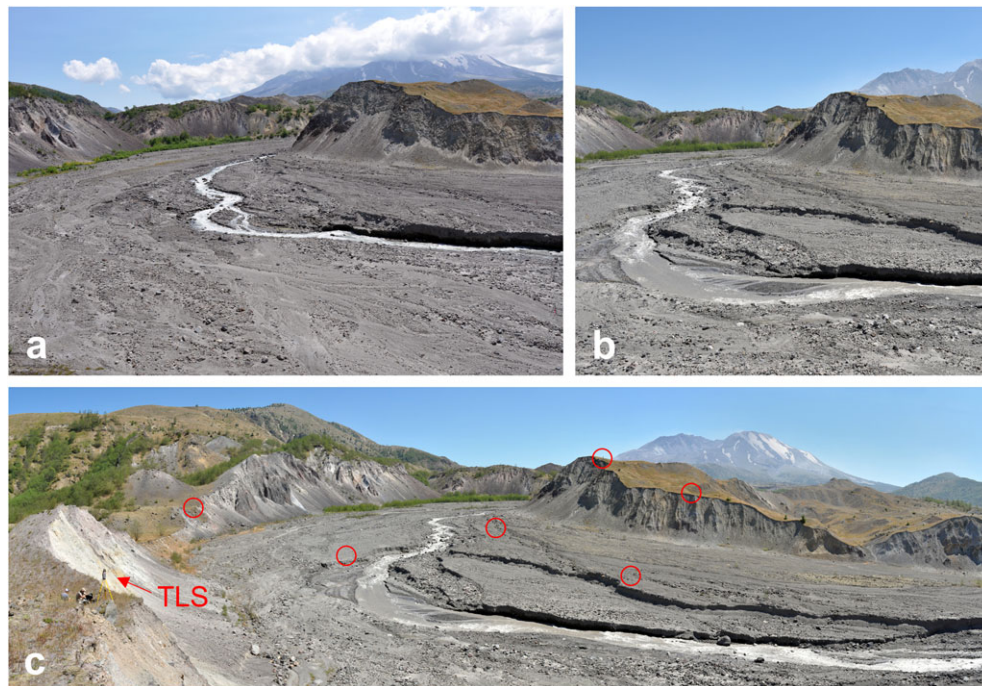


Figure 3. Photographs of North Fork Toutle River study reach on (a) August 3, 2010 and (b,c) August 14, 2012. A panoramic image (c) shows the TLS on the left of the frame (arrow); TLS target locations are circled in red. All views are looking upstream. [Colour figure can be viewed at wileyonlinelibrary.com]

360° but typically needs to be relocated multiple times to provide complete coverage of a study area. Similar to photogrammetry, tie-points (in this case targets placed throughout the area) and surveyed GCPs provide relative (internal) and absolute (external) orientation of the 3D point cloud.

We use TLS data acquired from Pitlick *et al.* (2010) in 2010 and 2011, using a tripod-mounted 122 kHz pulse scanner (Riegl VZ-400) from multiple ground positions at multiple elevations to minimize topographic occlusion and range while changing measurement incidence angle and surface reflectivity. These data had a GS distance < 5 cm. According to the manufacturer, the instrument had 5 mm range accuracy and 3 mm precision, and an angle resolution of 1.8 arcseconds. Stationary GNSS receivers, mounted above the scanner (Riegl) and two retroreflectors (Topcon), were used to georeference the TLS point clouds. Absolute accuracies of these GCPs was <5 cm (XYZ).

Airborne SfM surveys

Four SfM datasets were acquired from August 2010 to January 2014. Surveys were conducted within days of the 2010–2011 TLS surveys. We used a consumer-grade small-format DSLR camera system (Nikon D90; 12 MP, 380 mm² sensor, 12-bit ADC) with a fixed focal length lens (Nikon 20 mm f/2.8 AF-D) that has a hard focus stop at infinity to ensure optical stability. Our selection sought to maximize spatial resolution and dynamic range, while minimizing radial lens distortion and noise. Camera and lens configuration settings were selected to achieve the greatest information capacity of each dataset. The camera and lens system was upgraded in 2014 to improve image quality (Nikon D800E; 36 MP; 860 mm² sensor, 14-bit ADC; 50 mm f/1.8 AF-D lens).

Low-angle oblique photographs were captured handheld from the window of a manned helicopter 100–600 m above ground level at a ground speed <80 knots and in a convergent pattern. In these conditions, camera frame rate allowed >70% image overlap while encircling the study area. Average survey time was <5 minutes. With the hyperfocal distance easily exceeded, depth of field was not a concern so lens aperture was optimized (f/5.6–8.0 for these lenses) and the focus ring was taped at infinity to increase the

stability of the camera's internal geometry. Nominal GS distance was 2.6–3.0 cm for the 2010–2012 datasets and 4.2–6.5 cm for the 2014 dataset; though the camera system had greater resolution and longer focal length, the 2014 survey was flown at a greater object distance to evaluate the application of airborne SfM acquisition over Federal Aviation Administration (FAA)-restricted public lands.

Three-dimensional (3D) reconstruction and surface modeling

Topographic surface accuracy is a function of source data accuracy and characteristics (i.e. point density and distribution), surface interpolation method, and topographic roughness metrics (Li *et al.*, 2005). We focus our analysis on source data by using the same surface interpolation method for TLS and SfM data collected at the same location (i.e. same surface roughness). Independently georeferenced 3D point clouds produced by each method were imported into ArcGIS Desktop (Esri) to generate vector-based DTMs. DTMs were interpolated using Delaunay triangulation (e.g. Li *et al.*, 2005) to generate continuous 2.5D surfaces of non-overlapping triangular faces stored as triangulated irregular network (TIN)-based Esri terrain datasets. To avoid introducing additional variables into the error budget, points were not filtered (e.g. to classify ground-returns) because vegetation was not a significant issue, nor were they aggregated to a raster-based grid prior to analysis.

TLS-derived DTMs

Point clouds from individual TLS scan locations were merged and georeferenced using RiSCAN PRO (Riegl) software. Five retroreflector positions provided internal orientation of the model; static GNSS surveys of two of these retroreflectors and of the scanner at each location provided GCPs for external model orientation. Datum and coordinate system transformations converted ECEF coordinates to a

common reference frame, orthometric elevation, and planar coordinate system.

SfM-derived DTMs

We used VisualSfM software (free for non-commercial applications) to reconstruct 3D point clouds from the imagery. This software integrates scale invariant feature transform (SiftGPU) and multi-core bundle adjustment (Lowe, 2004; Wu, 2007, 2013; Wu *et al.*, 2011) as well as providing a graphical user interface to run patch-based and clustering multi-view stereo (PMVS/CMVS; Furukawa and Ponce, 2010). Compared to other prevalent open-source options, Bartoš *et al.* (2014) found VisualSfM to be most suitable for survey documentation due to its reliable results and ability to control key parameters within a largely automated workflow. Working on a moderately fast computer (64-bit, 4-core/8-thread 2.4 GHz CPU, 32 GB RAM, 2 GB GPU, SSD) the software produced >100 000 points per minute. We used a block invariant calibration model; our camera's internal geometry was fixed.

Prior to exporting a dense 3D point cloud, a simple seven-parameter (Helmert) least-squares transformation function (scale, rotation, translation) within VisualSfM was used to derive external orientation of the photogrammetric model, producing geodetic coordinates from the model's internal orientation. Transformation was accomplished by manually identifying four surveyed GCPs in the imagery (natural features on stable surfaces); absolute accuracies of these GNSS solutions were <9.8 cm horizontal (*XY*) and <12.5 cm vertical (*Z*). Similar to TLS data, datum and coordinate system transformations converted ECEF coordinates of the point cloud to a common reference frame, orthometric elevation, and planar coordinate system. In order to independently evaluate SfM-derived DTMs, we did not use GCPs to refine the camera-lens model, nor did we apply an iterative closest point algorithm to optimize the transformation compared to a pre-existing DTM.

Model evaluation methods

To examine the application of SfM to geomorphic change detection at our study site, we compare TLS- and SfM-derived DTMs to independent and higher-accuracy terrestrial topographic surveys (check points), then propagate spatially uniform error associated with each individual DTM to compute a morphological sediment budget for our study reach. This independent assessment of data referenced to a geodetic coordinate system allows us to assess absolute accuracy; many studies are limited to relative accuracy assessment because their benchmark dataset (e.g. TLS-DTM) is first used to georeference or transform their SfM-DTM.

Residual analysis

We evaluate surface model performance by comparison with total station and GNSS check points. Elevations of TLS- and SfM-derived DTMs are compared to datum- and geoid-adjusted ground check point elevations (Federal Geographic Data Committee [FGDC], 1998; Westaway *et al.*, 2003). We used a subset ($n=29-225$) of total check points, located in areas unchanged by geomorphic processes between the time of each survey, to compute summary DTM error statistics (Table I).

Residuals allow the computation of systematic and random errors, related respectively to survey accuracy and precision (Cooper and Cross, 1988). Accuracy is frequently reported as mean absolute error (MAE) or root-mean-square-error

Table I. Vertical digital terrain model (DTM) accuracies as compared to surveyed ground check point (CP) elevations

Method	Year	Precision			Accuracy		
		CP <i>n</i>	SDE (m)	MAE (m)	RMSE _{found} (m)	RMSE _{stated} (m)	
ALS	2009	103	0.36	0.25	± 0.18	± 0.04	
TLS	2010	171	0.72	0.15	± 0.37	± 0.01	
TLS	2011	225	0.56	0.02	± 0.48	± 0.01	
SfM	2010	164	0.87	0.36	± 0.45	± 0.97	
SfM	2011	200	0.83	0.34	± 0.42	± 0.80	
SfM	2012	88	0.77	0.37	± 0.39	± 0.61	
SfM	2014	39	0.55	0.06	± 0.28	± 0.05	

Note: standard deviation of error (SDE) is reported to the 95% confidence level (1.96σ); root-mean-square-error (RMSE) is reported as computed from this study (RMSE_{found}) and as reported by the vendor, software, or instrument manufacturer (RMSE_{stated}).

(RMSE), whereas the standard deviation of error (SDE or σ) provides estimates of precision (Greenwalt and Schultz, 1968; Westaway *et al.*, 2003; Li *et al.*, 2005). We express this uncertainty as both MAE and RMSE (Chai and Draxler, 2014) to facilitate comparison to other studies, but primarily draw our conclusions from resulting MAE which has been found by some to be more reliable and clearly interpreted (e.g. Willmott and Matsuura, 2005). MAE is an equally-weighted (linear) measurement of error, whereas RMSE measures the average magnitude of error using a quadratic function that is more sensitive to large values. Large differences between the two suggest a high degree of variance within error residuals. Accuracies of DTMs are often reported as single values (e.g. MAE or RMSE) without disaggregating horizontal (planimetric-*XY*) and vertical (altimetric-*Z*) components. When explicit, vertical error terms are more commonly reported, consistent with how topographic change detection maps are typically presented. In very rugged terrain, horizontal error is more closely coupled to vertical error.

Pairwise DTM comparison

Owing to increasing availability of repeat topographic surveys, geomorphic change is commonly analyzed by differencing DTMs (e.g. Lane *et al.*, 2003; Wheaton *et al.*, 2010; Anderson and Pitlick, 2014); a morphological sediment budget allows the estimation of spatially variable erosion and deposition. We produce spatially and temporally concurrent DoD by subtracting a DTM derived from a 2009 airborne LiDAR survey (30 cm GS distance; Mosbrucker, 2014) from TLS- and SfM-derived DTMs (2011). DoD volume is computed by geometric comparison between each surface using constrained Delaunay triangulation; the resulting height differential is represented by the *z*-values in the DoD. We assume there is no interaction between error sources and use simple error propagation to distinguish measurable volumetric change from inherent noise in each DoD. A minimum level of detection is computed using the root sum of squares from inherent error of each DTM (Bevington, 1969; Brasington *et al.*, 2003; Lane *et al.*, 2003; Bangen *et al.*, 2014). Changes below this level are discarded from the volume computation by applying a probabilistic threshold to each DoD at the 68% confidence interval. In our analysis, uncertainties are spatially uniform and SNR is high (e.g. Brasington *et al.*, 2000; Nouwakpo *et al.*, 2016), so we do not employ spatially variable estimates (e.g. Wheaton *et al.*, 2010).

Case study results

Our results show that vertical accuracies of DTMs derived from SfM photogrammetry (0.06–0.37 m) and LiDAR can be of the same approximate magnitude (Table I, MAE). Point densities (6.0–17.3 m⁻²) would support the generation of gridded models (i.e. DEMs) with cell sizes (1.0–1.6 m) equal to or greater than airborne LiDAR (Table II). Though less precise (0.55–0.87 m), SfM produced less variation in error residuals than LiDAR (Table I, compare MAE to RMSE_{found}) suggesting a relative lack of large outliers within the SfM data, despite being unfiltered.

Volumetric change computed from spatially and temporally concurrent TLS- and SfM-derived DTMs (Figure 4) differ by ~10% and are within analysis uncertainty (Table III). Apparent average volume of erosion computed from both methods is 112 300 ± 20 950 m³ over the three-year period. No significant deposition was observed in the field but there is likely small areas of local deposition not detected in the DoDs; deposition volume below the minimum level of detection was much greater for the SfM-ALS DoD than the TLS-ALS DoD. For these data, the minimum level of detection used to threshold each DoD is 0.46–0.51 m. DoD averages are -0.26 m for the SfM-ALS DoD and -1.48 m for the TLS-ALS DoD. With these methods, we were unable to detect significant changes over >80% of the study area, which is consistent with field observations. The standard deviation of the SfM-ALS DoD is almost four times less than that of the TLS-ALS DoD, suggesting a better overall fit to the 2009 ALS-derived DTM.

According to laboratory analyses (DxO Labs; <http://dxomark.com>), upgrading the camera system in 2014 increased resolution by 300% (340% effective), sensor size by >240%, and dynamic range by 360%. Noise was reduced by 300% and lens distortion by 800%. Little change to absolute vertical accuracy and precision of individual SfM-derived DTMs was observed prior to this upgrade (< 8% variation in accuracy and 13% increase in precision between 2010 and 2012). Increasing quantitative image quality in 2014 produced an eight-fold increase in the number of 3D points generated per frame (Table II). We found a statistically-significant correlations between accuracy ($R^2 = 0.99$) and precision ($R^2 = 0.90$) predicted by number of points per frame; the 2014 DTM was six times more accurate and 50% more precise than 2010–2012 averages (Table I) despite a two-fold increase in GS distance and a six-fold reduction in the number of images used during reconstruction. Uncertainty/distance values were 1:270–294 for 2010–2012 surveys and 1:10 160 for 2014.

We did not detect a deformation pattern in our SfM-derived DTMs. All four years used multiscale imagery acquired at convergent angles. Furthermore, we ensured our camera system had fixed internal geometry and were able to define this in VisualSfM, which may have also contributed to the lack of distortion in our results. Experience at other sites, where long strips of parallel imagery resulted in doming, shows that correcting radial lens distortion in Adobe Photoshop (and disabling this correction in VisualSfM) significantly reduced this systematic error, reduced processing time (~10%), and generated the same number of points per frame.

Table II. Digital terrain model (DTM) summary statistics for study area

Method	Date	Source	DTM point characteristics				
			Points <i>n</i>	Pt./frame <i>n</i>	Pt. ρ (m ⁻²)	Pt. <i>d</i> (m)	Cell size (m)
ALS	September 2009	2 passes	705 168	—	6.70	0.39	1.55
TLS	August 2010	6 scans	29 170 321	—	277.04	0.06	0.24
TLS	August 2011	8 scans	84 392 273	—	801.51	0.04	0.14
SfM	August 2010	211 photos	1 816 408	8609	17.25	0.24	1.00
SfM	August 2011	76 photos	807 421	10 624	7.67	0.36	1.44
SfM	August 2012	81 photos	625 018	7716	5.94	0.41	1.64
SfM	January 2014	20 photos	1 397 229	69 861	13.27	0.27	1.10

Note: Average point spacing (Pt. *d*) is the square root of the inverse of average point density (Pt. ρ). Supported cell size (if data are gridded) is Pt. *d* multiplied by four.

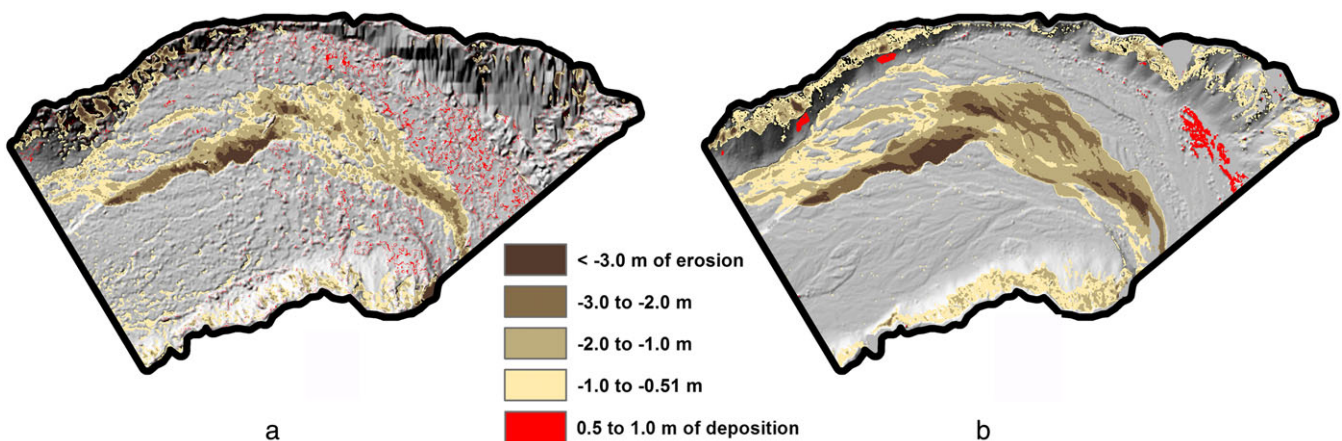


Figure 4. Digital terrain models of difference (DoD) results. Both (a) SfM-ALS and (b) TLS-ALS DoDs are shown with their respective minimum level of detection (LoD_{min}) threshold applied. [Colour figure can be viewed at wileyonlinelibrary.com]

Table III. Digital terrain models of difference (DoD) results

DoD period ($t_1 - t_0$)	LoD _{min} (m)	Δ Mean (m)	Δ SD (m)	Volume of erosion (m ³)	Volume of deposition (m ³)
2011 SfM – 2009 ALS	0.46	–0.26	2.96	106 300 ± 16 400	2520 ± 13 460
2011 TLS – 2009 ALS	0.51	–1.48	10.54	118 300 ± 25 500	453 ± 5

Note: DoDs were computed by subtracting a pre-surface (t_0) from a post-surface (t_1). Minimum level of detection (LoD_{min}) threshold was applied to the absolute value of elevation (Z), centered around zero. Mean elevation difference (Δ Mean) and associated standard deviation (Δ SD) at the 95% confidence level (1.96σ) was computed with threshold applied. Volume of deposition may include vegetation growth. Analysis uncertainty (\pm) is provided for each volume estimate.

Correlation of Image Optimization to Accuracy of SfM-derived DTMs

Review methods

Comparing SfM-derived topographic data to more established methods (e.g. total station, GNSS, ALS, TLS) provides confidence to use these data for process-oriented analyses (Smith *et al.*, 2016). The flexibility of SfM promotes a lack of consistency in both workflow and validation which challenges efforts to isolate sources of error. A comprehensive error budget requires a robust experiment in a controlled environment (Smith and Vericat, 2015); instead, our comparison investigates overall trends to deconstruct the principle components of a SfM error budget.

We build upon previous synthesis efforts by compiling accuracies of 67 SfM-derived DTM datasets and their associated survey metrics from 16 validation studies (published 2012–2015) (Table IV). Studies employ a variety of camera systems, but quantitative image quality metrics for each (i.e. effective resolution, dynamic range, noise, distortion) are not computed due to lack of information. Instead, we use three available surrogates: sensor size, focal length, and lens type.

Ordinary least squares regression models describe the covariability of these surrogates (and other explanatory variables) and are used to evaluate the ability to predict accuracy of SfM-derived DTMs (response variable). We evaluate the quality of fit and significance of the relationships by checking for non-linearity, heteroscedasticity (i.e. non-constant variability of the residuals), normality of residuals, and the coefficient of determination (R^2). The two strongest models are presented; both models benefited from base-10 logarithmic transformation to improve these metrics.

Review results

While the majority of studies we reviewed reported vertical error statistics only (horizontal assessment is rare in the literature), there are fundamental differences in both the type of assessment and summary statistics reported. Half of the datasets (49%) assess relative, rather than absolute, accuracy; almost all of these relative-accuracy studies use an ICP algorithm to align SfM point cloud to a TLS survey prior to assessing the accuracy of SfM data using the same TLS as the benchmark. Relative accuracy is two times greater (9.9 cm average MAE, $n=26$) than absolute accuracy (21.6 cm average MAE, $n=36$). MAE is more common ($n=62$) than RMSE ($n=39$) and both metrics are reported for 25 datasets; average RMSE (± 34.7 cm) is double average MAE (16.7 cm).

The two most common software packages used are Agisoft Photoscan and Autodesk 123D Catch; their prevalent use further complicates the evaluation of an error budget. Photoscan provides a means to optimize a reconstruction based on GCPs,

analogous to traditional photogrammetry (i.e. pseudo-SfM). Thoeni *et al.* (2014) found the use of an optimization routine in Photoscan (to remove the non-linear component of the transformation) reduced GCP error by 63–98%, with the greatest improvement being for low-quality camera systems. Every study that uses Photoscan (except Townsend [2013] and Javernick *et al.* [2014]) utilizes this optimization routine, which mitigates non-linear distortion and corrects some aspects of low image quality. In contrast, Autodesk's 123D Catch, a web-based service, reduces image quality to improve processing time at the expense of accuracy.

Our review found a 64% degradation related to lens type (invariant of assessment type); average MAE for fixed lenses is 6.5 cm compared to 18.1 cm for zoom lenses. Results show no universal correlation between accuracy and sensor size or focal length. The three surrogates are well represented; 63% of datasets have sensors >300 mm² (15 to 862 mm² range; 230 mm² mean), focal length ranges from 17 to 81 mm (equivalent) with a mean of 34 mm, and 43% of reviewed datasets use fixed focal length (rather than zoom) lenses.

Despite the importance of image quality and other parameters, our review suggests that scale is the most universal explanatory variable in a SfM error budget. Object distance ranges from 0.7 to 1400 m (180 m average, $n=49$), corresponding to uncertainty/distance ratios of 1:67–1:200 000 (1:6600 average, $n=52$; 1:1500 average if two outliers are removed) (Table IV; uncertainty/distance MAE). Our regression model predicting accuracy (MAE) from object distance for both types of accuracy assessment (relative and absolute) shows a statistically significant relationship between the two variables (by t -statistic and p -value at 95% confidence interval). The model explains 54% of the variability in MAE. Probability plot correlation coefficient ($R^2=0.85$) indicates that residuals have a homoscedastic pattern and near-normal distribution. Standard errors of intercept and slope are 0.23 and 0.13 respectively. The model, $\log_{10}(\text{MAE}) = -0.92 + 0.93\log_{10}(\text{distance})$, can be retransformed and corrected for associated bias if needed.

Our model using GS distance is slightly better at predicting MAE. For the datasets reviewed, GS distance ranges from 0.01 to 23.5 cm (3.8 cm average, $n=46$). The model predicts accuracy (MAE) from GS distance for both types of accuracy assessment, shows a statistically significant relationship between the two variables and explains 68% of the variability in MAE. Probability plot correlation coefficient ($R^2=0.84$) indicates that residuals have a homoscedastic pattern and near-normal distribution, with standard errors of intercept and slope at 0.10 and 0.11 respectively. The model is: $\log_{10}(\text{MAE}) = -0.51 + 1.12\log_{10}(\text{GS distance})$.

Discussion

Several factors constrain the utility and accuracy of SfM-derived DTMs. These include scale and quality of the

Table IV. Comparison of selected accuracy results of SfM-derived digital terrain models (DTMs)

Study	Camera			Geodetic control points			Accuracy assessment			MAE			RMSE			Uncertainty: distance ^b			Normalized by GS ^b						
	Platform	Sensor Size (mm ²)	Focal length ^a (mm)	Lens type	Nominal GS ^b (cm)	Images n	Software	Points n	Source	Type	Points n	Benchmark	XYZ ^c (cm)	XY (cm)	Z (cm)	XYZ ^c (cm)	XY (cm)	Z (cm)	MAE	RMSE	MAE	RMSE	MAE	RMSE	
Rosnell and Honkavaara, 2012	Aerial	43	28	Fixed	2.5	280	iWitness, Microsoft Photosynth	14	S-GNSS	Relative	14	Software estimate	—	—	—	60	—	—	—	—	117	—	—	—	24.0
Rosnell and Honkavaara, 2012	Aerial	225	42	Fixed	2.6	251	Microsoft Photosynth	31	TS, TP-DTM	Absolute	grid	same TP	—	—	—	—	—	150	—	—	83	—	—	—	57.7
Castillo <i>et al.</i> , 2012	Terrestrial	329	—	—	2	191	Bundler ^c	6	GNSS ICP, TLS	Absolute	grid	TLS	—	—	—	—	—	—	—	233	—	—	—	—	1.5
James and Robson, 2012	Terrestrial	329	81	Fixed	0.01	92	Bundler ^c	4	point cloud	Relative	cloud	same TLS	0.01	—	—	0.03	—	—	—	7821	2333	1.2	—	—	4.1
James and Robson, 2012	Aerial	343	32	Fixed	37.1	89	Bundler ^c	45	M-GNSS	Absolute	grid	CRP; VMS-Gotcha	—	—	—	—	—	78	—	—	1282	—	—	—	2.1
James and Robson, 2012	Terrestrial	329	45	Fixed	0.4	143	Bundler ^c	8	TLS point cloud	Relative	grid	same TLS	—	—	—	—	—	2.1	—	—	952	—	—	—	5.6
Fonstad <i>et al.</i> , 2013	Aerial	28	37	Variable	5	304	Microsoft Photosynth	10	M-GNSS	Absolute	15	M-GNSS	—	4	7	—	—	—	—	571	—	—	—	—	1.4
Fonstad <i>et al.</i> , 2013	Aerial	28	37	Variable	5	304	Microsoft Photosynth	10	M-GNSS	Absolute	cloud	ALS	—	—	—	—	—	—	—	67	—	—	—	—	12.0
Townsend, 2013	Aerial	367	53	Variable	1.2	70	Agisoft Photoscan <i>not optimized</i>	8	M-GNSS, ALS	Relative	7	Software estimate	—	32	80	—	—	99	89	104	93	66.7	—	—	74.2
Welly <i>et al.</i> , 2013	Aerial	372	—	—	—	383	Bundler ^c	383	R-GNSS ICP, TLS	Absolute	grid	TP	—	—	—	—	—	—	—	1818	—	—	—	—	—
James and Quinton, 2014	Terrestrial	329	45	Fixed	0.5	87	Bundler ^c	8	point cloud	Relative	cloud	same TLS	1.44	—	—	1.78	—	—	—	1736	1404	3.1	—	—	3.8
Gómez-Gutiérrez <i>et al.</i> , 2014	Terrestrial	332	—	Variable	—	93	Autodesk 123D Catch ^d	10	point cloud	Relative	cloud	same TLS	2.5	—	—	—	—	—	—	372	—	—	—	—	—
Gómez-Gutiérrez <i>et al.</i> , 2014	Terrestrial	332	—	Variable	—	93	Autodesk 123D Catch ^d	10	point cloud	Relative	grid	same TLS	—	—	—	—	—	4.7	—	—	—	—	—	—	—
Gómez-Gutiérrez <i>et al.</i> , 2014	Terrestrial	332	—	Variable	—	66	Autodesk 123D Catch ^d	10	point cloud	Relative	cloud	same TLS	0.9	—	—	—	—	—	—	1167	—	—	—	—	—
Gómez-Gutiérrez <i>et al.</i> , 2014	Terrestrial	332	—	Variable	—	66	Autodesk 123D Catch ^d	10	point cloud	Relative	grid	same TLS	—	—	—	—	—	—	—	—	—	—	—	—	—
Gómez-Gutiérrez <i>et al.</i> , 2014	Terrestrial	332	—	Variable	—	73	Autodesk 123D Catch ^d	10	point cloud	Relative	cloud	same TLS	2.4	—	—	—	—	—	—	404	—	—	—	—	—

(Continues)

Table IV. (Continued)

Study	Camera			Geodetic control points			Accuracy assessment			MAE			RMSE			Uncertainty: distance ^g			Normalized by GS ^h						
	Platform	Sensor Size (mm ²)	Focal length ^a (mm)	Lens type	Nominal GS ^b (cm)	Images n	Software	Points n	Source	Type	Points n	Benchmark	XYZ ^c (cm)	XY (cm)	Z (cm)	XYZ ^d (cm)	XY (cm)	Z (cm)	MAE	RMSE	MAE	RMSE	MAE	RMSE	
Micheletti <i>et al.</i> , 2015b	Terrestrial	368	53	Fixed	0.3	13	Autodesk 123D Catch ^d	10	ICP, TLS point cloud	Relative	cloud	same TLS	0.5	—	—	—	—	—	—	1887	—	—	—	1.8	—
Micheletti <i>et al.</i> , 2015b	Terrestrial	368	53	Fixed	0.3	13	Autodesk 123D Catch ^d	10	ICP, TLS point cloud	Relative	grid	same TLS	—	—	—	—	—	—	1.7	—	—	—	595	—	5.6
Micheletti <i>et al.</i> , 2015b	Terrestrial	15	29	Fixed	0.6	13	Autodesk 123D Catch ^d	10	TLS point cloud	Relative	cloud	same TLS	2.1	—	—	—	—	—	—	483	—	—	—	3.5	—
Micheletti <i>et al.</i> , 2015b	Terrestrial	15	29	Fixed	0.6	13	Autodesk 123D Catch ^d	10	TLS point cloud	Relative	grid	same TLS	—	—	—	—	—	—	5.0	—	—	—	199	—	8.4
Micheletti <i>et al.</i> , 2015b	Terrestrial	15	29	Fixed	0.6	13	Autodesk 123D Catch ^d	10	ICP, TLS point cloud	Relative	cloud	same TLS	1.1	—	—	—	—	—	—	952	—	—	—	1.8	—
Micheletti <i>et al.</i> , 2015b	Terrestrial	15	29	Fixed	0.6	13	Autodesk 123D Catch ^d	10	ICP, TLS point cloud	Relative	grid	same TLS	—	—	—	—	—	—	3.1	—	—	—	327	—	5.1
Micheletti <i>et al.</i> , 2015b	Terrestrial	15	29	Fixed	23.5	13	Autodesk 123D Catch ^d	8	TLS point cloud	Relative	cloud	same TLS	68.9	—	—	—	—	—	—	580	—	—	—	2.9	—
Micheletti <i>et al.</i> , 2015b	Terrestrial	15	29	Fixed	23.5	13	Autodesk 123D Catch ^d	8	ICP, TLS point cloud	Relative	cloud	same TLS	52.6	—	—	—	—	—	—	760	—	—	—	2.2	—
Vericat, 2015 Smith and Smith	Aerial	28	29	Variable	1.7	350	Agisoft Photoscan ^e	30	S-GNSS	Absolute	grid	TLS	—	—	21.8	—	—	30.8	—	216	153	12.8	12.8	18.1	—
Vericat, 2015 Smith and Smith	Terrestrial	25	25	Variable	0.2	25–33	Agisoft Photoscan ^e	5	S-GNSS, TS	Absolute	9–36	TS	—	—	2.8	—	—	3.7	—	177	1260	14.2	18.7	—	—
Vericat, 2015 Smith and Smith	Terrestrial	25	25	Variable	0.2	25–33	Agisoft Photoscan ^e	5	S-GNSS, TS	Absolute	grid	TLS	—	—	0.9	—	—	1.3	—	543	3672	4.6	6.4	—	—
Vericat, 2015 Smith and Smith	Terrestrial	25	25	Variable	—	—	Agisoft Photoscan ^e	30	S-GNSS	Absolute	grid	TLS	—	—	10.1	—	—	18.3	—	—	—	—	—	—	—
Vericat, 2015 Smith and Smith	Terrestrial	25	25	Variable	—	—	Agisoft Photoscan ^e	30	S-GNSS	Absolute	504	TS	—	—	10.2	—	—	18.3	—	—	—	—	—	—	—
Vericat, 2015 Smith and Smith	Aerial	356	25	Variable	2.2	149	Agisoft Photoscan ^e	30	S-GNSS	Absolute	515	TS	—	—	6.6	—	—	9.9	1061	707	3.0	4.5	—	—	
Vericat, 2015 Smith and Smith	Aerial	356	25	Variable	2.2	149	Agisoft Photoscan ^e	30	S-GNSS	Absolute	grid	TLS	—	—	5.5	—	—	8.0	1273	875	2.5	3.6	—	—	
Vericat, 2015 Smith and Smith	Aerial	356	25	Variable	5.3	527	Agisoft Photoscan ^e	30	S-GNSS	Absolute	515	vs. TS	—	—	12.1	—	—	18.2	1405	934	2.3	3.4	—	—	
Vericat, 2015 Smith and Smith	Aerial	356	25	Variable	5.3	527	Agisoft Photoscan ^e	30	S-GNSS	Absolute	730	vs. TS	—	—	29.8	—	—	44.5	570	382	5.6	8.4	—	—	
Vericat, 2015 Smith and Smith	Aerial	356	25	Variable	5.3	527	Agisoft Photoscan ^e	30	S-GNSS	Absolute	grid	TLS	—	—	10.9	—	—	15.4	1560	1104	2.1	2.9	—	—	
Vericat, 2015 Smith and Smith	Aerial	356	25	Variable	8.4	138	Agisoft Photoscan ^e	30	S-GNSS	Absolute	515	vs. TS	—	—	18.1	—	—	27.9	1492	968	2.2	3.3	—	—	

(Continues)

Table IV. (Continued)

Study	Camera			Geodetic control points			Accuracy assessment			Uncertainty: distance ^g			Normalized by GS ^h											
	Platform	Sensor Size (mm ²)	Focal length ^a (mm)	Lens type	Nominal GS ^b (cm)	Images n	Software	Points n	Source	Type	Points n	Benchmark	XYZ ^c (cm)	XY (cm)	Z (cm)	RMSE (cm)	XYZ ^c (cm)	XY (cm)	Z (cm)	RMSE (cm)	MAE (cm)	RMSE (cm)	MAE (cm)	RMSE (cm)
Smith and Vericat, 2015	Aerial	356	25	Variable	8.4	138	Agisoft Photoscan ^e	30	S-GNSS	Absolute	730	1.0 m grid vs. TS	—	—	27.3	—	—	—	—	39.1	989	691	3.3	4.7
Smith and Vericat, 2015	Aerial	356	25	Variable	8.4	138	Agisoft Photoscan ^e	30	S-GNSS, TS, ICP	Absolute	grid	TLS	—	—	20.8	—	—	—	—	37.4	1298	722	2.5	4.5
Nouwakpo <i>et al.</i> , 2016	Terrestrial	329	32	Fixed	0.06	25	Agisoft Photoscan ^e	10–15	TLS point cloud, TS, ICP	Relative	grid	same TLS	—	—	0.003	—	—	—	—	—	66667	—	0.1	—
Nouwakpo <i>et al.</i> , 2016	Terrestrial	329	32	Fixed	0.06	127	Agisoft Photoscan ^e	10–15	TLS point cloud, TS, ICP	Relative	grid	same TLS	—	—	0.047	—	—	—	—	—	4255	—	0.8	—
Nouwakpo <i>et al.</i> , 2016	Terrestrial	329	32	Fixed	0.06	72	Agisoft Photoscan ^e	10–15	TLS point cloud, TS, ICP	Relative	grid	same TLS	—	—	0.108	—	—	—	—	—	1852	—	1.8	—
Nouwakpo <i>et al.</i> , 2016	Terrestrial	329	32	Fixed	0.06	143	Agisoft Photoscan ^e	10–15	TLS point cloud, TS, ICP	Relative	grid	same TLS	—	—	0.001	—	—	—	—	—	200000	—	0.0	—
Nouwakpo <i>et al.</i> , 2016	Terrestrial	329	32	Fixed	0.06	282	Agisoft Photoscan ^e	10–15	TLS point cloud, TS, ICP	Relative	grid	same TLS	—	—	2.830	—	—	—	—	—	71	—	47.2	—
Nouwakpo <i>et al.</i> , 2016	Terrestrial	329	32	Fixed	0.06	145	Agisoft Photoscan ^e	10–15	TLS point cloud	Relative	grid	same TLS	—	—	0.990	—	—	—	—	—	202	—	16.5	—
Dietrich, 2016	Aerial	332	25	Variable	6	1483	Agisoft Photoscan ^e	66	M-GNSS, M- and S-GNSS	Absolute	56	ALS-point cloud	—	—	49	53	—	62	73	377	274	8.8	12.2	
This study, 2010 dataset	Aerial	384	30	Fixed	2.8	211	VisualSfM	4	M- and S-GNSS	Absolute	164	M- and S-GNSS, TS	—	—	36	—	—	—	45	278	222	12.9	16.1	
This study, 2011 dataset	Aerial	384	30	Fixed	2.8	76	VisualSfM	4	M- and S-GNSS	Absolute	200	M- and S-GNSS, TS	—	—	34	—	—	—	42	294	238	12.1	15.0	
This study, 2012 dataset	Aerial	384	30	Fixed	2.8	81	VisualSfM	4	M- and S-GNSS	Absolute	88	M- and S-GNSS, TS	—	—	37	—	—	—	39	270	256	13.2	13.9	
This study, 2014 dataset	Aerial	862	50	Fixed	5.4	20	VisualSfM	4	M- and S-GNSS	Absolute	39	M- and S-GNSS, TS	—	—	6	—	—	—	28	10160	2143	1.1	5.2	

Note: Unless provided in the literature, nominal ground sample (GS) distance is estimated based on sensor characteristics, lens focal length, and object distance. Geodetic control is provided by: recreation-grade GNSS (R-GNSS, ±3.0 m), map-grade GNSS (M-GNSS, ±0.50 m), survey-grade GNSS (S-GNSS, ±0.10 m), total station (TS, ±0.05 m), or a pre-existing DTM (e.g. traditional photogrammetric (TP)- or TLS-DTM). Absolute accuracy is assessed by independent validation points or DTMs (e.g. GNSS); relative accuracy is assessed by comparison with another DTM or estimated by software (often based on GCP residuals or proprietary bundle-adjustment quality thresholds).

^aFocal length is stated in 35 mm equivalent.

^bNominal GS distance is calculated using average distance to subject, focal length, sensor size, and pixel dimensions. Actual GS distance is variable throughout the frame of an oblique image.

^cBundler is comprised of SIFT, CMVS, PMVS2, and SfM_georef.

^dAutodesk 123D Catch downsamples imagery to three megapixels to decrease processing time.

^eHas been optimized within Agisoft Photoscan to include ground control points in the final reconstruction, similar to traditional photogrammetry.

^fAssumed to be three-dimensional (3D) (XYZ) when unspecified in report

^gBased on vertical (Z); where Z is not available, this value is based on 3D (XYZ) accuracy.

photographs, lighting conditions, pixel matching performance, camera calibration quality, point density, GCP characteristics and transformation, terrain characteristics, and DTM surface interpolation method.

Despite our case study results showing a strong correlation between image quality and accuracy, our literature review shows no universal correlation between sensor size and accuracy. This is presumably due to ambiguity in the comparison, as larger sensors have been shown to have better image quality (greater dynamic range and lower noise), especially in challenging ambient lighting conditions, where Gienko and Terry (2014) found a reduction in point density by a factor of 170. Unfortunately, the studies we reviewed lacked information necessary to sufficiently evaluate point density.

Our results support experiments conducted by Shortis *et al.* (2006) who show that while zoom lenses can produce acceptable results, a fixed focal length lens provides superior accuracy, precision, and stability; their results show degradation of relative precision (72% average RMS) and accuracy (44% average RMS) using zoom compared to fixed lenses.

While Micheletti *et al.* (2015a) suggested that a greater number of photographs could increase point density, our experience instead supports Gomez *et al.* (2015), who found it better to have fewer high-quality images rather than a large number of low-quality frames. Our review shows no correlation between the number of photographs used in SfM reconstruction and resulting DTM accuracy.

The relationship between photographic scale and accuracy of photogrammetric data is well established. However, unlike standard large-format metric camera systems used for traditional photogrammetry, SfM source imagery is typically acquired using small-format consumer-grade digital cameras which use a variety of different sensors and lenses. This lack of standardized camera system causes photographic scale to be determined by more than object distance. While recent SfM literature describes scale as object distance, we found GS distance, or spatial resolution of the imagery, to be a better metric.

Our simple linear regression model predicting MAE from object distance ($R^2=0.54$, $n=52$) is slightly weaker than a power law found by a previous review of existing SfM validation datasets by Smith and Vericat (2015) over a comparable range (0.57 exponent, $R^2=0.69$, $n=28$). Our model predicting MAE from GS distance of reviewed datasets is comparable ($R^2=0.68$, $n=46$) but more applicable considering how photographic scale is calculated from consumer-grade digital camera systems. It is important to note that none of these models fully describe the multivariate relationships within a complex SfM error budget; correlations do, however, provide a useful contribution to the discipline and promote further investigation.

In a similar attempt to relate image quality to accuracy, Eltner *et al.* (2016) evaluated absolute pixel size as a reasonable surrogate but did not extend their analysis to GS distance (i.e. pixel size projected onto the ground surface). Their review found no obvious influence of pixel size on SfM-derived DEM quality due to many cameras having similar values ($\sim 5 \mu\text{m}$) producing a large range of errors.

We build upon this discussion and practical guidelines previously synthesized (e.g. Smith *et al.*, 2016), specifically regarding the use of photographic instruments for geomorphic applications of SfM; these are summarized as follows:

Camera system selection:

- Large ($\geq 300 \text{ mm}^2$, or APS-C) high-resolution (≥ 16 MP) sensor that has no anti-aliasing filter effect and is coupled to a ≥ 14 -bit non-linear ADC.

- Stable and fixed lens (non-retractable and non-zoom) with a focal length between 35 and 105 mm, preferably with a mechanical stop at infinity.
- Lens with apochromatic optical formula that includes low dispersion and/or aspheric glass.
- Camera body and lens made of rigid metal (magnesium is common).
- A few compact camera systems are available that meet most of these guidelines if size/weight are restricted (e.g. UAV platforms).

Camera system configuration:

- For stationary camera platforms, set the exposure mode to aperture priority and select an aperture of $f/5.6$ – 11.0 .
- For non-stationary camera platforms (e.g. aerial surveys), set the exposure mode to shutter priority and select a shutter speed $< 1/400$ s.
- Keep ISO as low as possible (≤ 400) while maintaining acceptable shutter speed and aperture values.
- Set the camera and/or lens to manual focus (at an appropriate distance for optimal depth-of-field if hyperfocal distance is not exceeded) and tape the focus ring.
- Disable image stabilization, automatic image rotation, and (generally) in-camera distortion correction.
- Set the camera to record RAW and fine JPEG at the maximum available resolution and AdobeRGB color space if read/write speed is not limited.

Image acquisition:

- Mission plan to ensure optimum ambient lighting conditions; choose an overcast day or center survey interval on solar noon (online calculators available).
- Ensure all areas of interest are included in \geq three photographs.
- Minimize GS distance (image spatial resolution) by using a short object distance or longer focal length for a given sensor size.
- Prioritize image quality over quantity; acquire the minimum number of photographs needed to capture the study area spatial extent and avoid occlusions at a given GS distance.
- Acquire convergent imagery ($< 20^\circ$ camera-to-camera) with $> 40^\circ$ angle of incidence (camera-to-ground) at multiple object distances, with $\geq 80\%$ frame overlap (the entire study area supplemented by detailed imagery at greater scale); if a parallel strip is necessary, consider correcting radial lens distortion in Photoshop prior to reconstruction and/or subdividing the project if sufficient GCPs are present.
- If the dynamic range of a static scene is too great, consider capturing multiple frames at different exposures to produce an HDR image.
- If significant reflections or glare are present (e.g. water surface), consider using a polarizing filter on the lens (only useful and right angles to the sun however).

Our experience has shown that computer hardware characteristics, largely overlooked by the SfM community, are related to the number of features matched per frame, and thus resulting model accuracy. Increasing the information capacity (specifically resolution and bit-depth) of SfM source imagery can greatly influence the computational requirements of 3D reconstruction. Because many SfM algorithms are designed to use high-end computer graphics cards and parallel processing, the CPU, RAM, power supply, and cooling system of a SfM workstation (or cluster) should support heavy computation. This is especially important as camera systems

continue to increase image file size; unpublished aerial surveys conducted by the authors regularly exceed 30 GB per 10 river miles.

Conclusions

This paper provided a practical discussion of camera system selection, configuration, and image acquisition considerations for SfM photogrammetric applications in geomorphology. The hypothesis that optimizing source imagery could increase DTM accuracy was tested by evaluating accuracies of four SfM datasets conducted over multiple years of a gravel bed river floodplain using independent topographic survey points. This analysis was then extended to compare morphological sediment budgets computed from SfM- and LiDAR-derived DTMs. Case study results were compared to existing SfM validation studies in an attempt to deconstruct the principle components of a SfM error budget.

The premise of this paper is that pixel-level feature detection is a key constraint to SfM camera calibration, point density, and resulting DTM accuracy. This pixel matching is a function of image characteristics (e.g. information capacity, geometry, lighting, and surface texture). Case study results show an eight-fold increase in number of points generated from each frame, a six-fold increase in vertical accuracy, and 50% greater precision produced by increasing the information capacity of source imagery. These DTMs have point densities ($6\text{--}17\text{ m}^{-2}$) and accuracies ($6\text{--}37\text{ cm}$) of the same approximate magnitude as airborne or terrestrial LiDAR, though precision is found to be less ($55\text{--}87\text{ cm}$). When propagated through volumetric change analysis, individual DTM accuracy was sufficient to detect moderate geomorphic change (order $100\,000\text{ m}^3$) on an unvegetated fluvial surface; change detection determined from repeat LiDAR and SfM surveys differed by about 10% and was within analysis uncertainty.

The accuracies of 67 published SfM datasets and their associated survey metrics were evaluated, despite being challenged by many ambiguities (e.g. assessment type, software, lack of metadata) which severely limited comparison to case study results regarding image quality parameters. No significant relationship between DTM accuracy and sensor size, focal length, number of frames, or GCP quantity was found. However, the review showed that using a fixed focal length, rather than a zoom, lens significantly improved (64%) mean absolute vertical accuracy of these datasets.

Despite the importance of image quality, our review suggests that scale is the most universal explanatory variable in a SfM error budget. While recent SfM literature describes scale as object distance, we found GS distance, or spatial resolution of the imagery, to be a better metric, accounting for 68% of the variability in MAE. We argue that ground sample distance is a more applicable considering how photographic scale is calculated from consumer-grade digital camera systems.

These findings are used to synthesize the current best practices regarding the use of photographic instruments for geomorphic applications of SfM. Our observations support the need for rigorous laboratory-based investigations of image optimization to advance the art and science of making measurements from photographs.

Acknowledgments—The authors thank the USGS Volcano Hazards Program, UNAVCO, and the University of Colorado for supporting this work. The authors thank Tami Christianson (CVO) for her data-wrangling skills, colleagues at CVO (Steve Schilling, Matt Logan,

Rob Wardwell, Rick LaHusen, Kelly Swinford) for technical advice and inspiration, UNAVCO (Jim Normandeau, Chuck Meertens, Keith Williams, and Ken Austin) for acquisition support, J.L. Aviation (Jeff Linscott and Pete Emerson) for top-notch flight service, and the USACE (Paul Sclafani, Jacob MacDonald, Chris Nygaard) for generously sharing their data. The manuscript was greatly improved through comprehensive evaluations by Joe Wheaton and an anonymous reviewer. Any use of trade, firm, or product names is for descriptive purposes only and does not imply endorsement by the US Government.

References

- Anderson S, Pitlick J. 2014. Using repeat LiDAR to estimate sediment transport in a steep stream. *Journal of Geophysical Research - Earth Surface* **119**: 621–643. DOI:10.1002/2013JF002933.
- Bangen S, Wheaton J, Bouwes N, Jordan C, Volk C, Ward MB. 2014. Crew variability in topographic surveys for monitoring wadeable streams: a case study from the Columbia River Basin. *Earth Surface Processes and Landforms* **39**(15): 2070–2086. DOI:10.1002/esp.3600.
- Bartoš K, Pukanská K, Sabová J. 2014. Overview of available open-source photogrammetric software, its use and analysis. *International Journal for Innovation Education and Research* **2**(4): 62–70.
- Bevington R. 1969. *Data Reduction and Error Analysis for the Physical Sciences*. McGraw-Hill: New York.
- Brasington J, Rumsby BT, McVey RA. 2000. Monitoring and modelling morphological change in a braided gravel-bed river using high resolution GPS-based survey. *Earth Surface Processes and Landforms* **25**: 973–990.
- Brasington J, Langham J, Rumsby B. 2003. Methodological sensitivity of morphometric estimates of coarse fluvial sediment transport. *Geomorphology* **53**: 299–316. DOI:10.1016/S0169-555X(02)00320-3.
- Buckley SJ, Mills JP, Mitchell HL. 2004. Improving the accuracy of photogrammetric absolute orientation using surface matching. *Proceedings of the ISPRS Congress: Technical Commission III*, Istanbul, Turkey, 12–23 July; 30–35.
- Cao F, Guichard F, Hornung H. 2010. Information capacity: a measure of potential image quality of a digital camera. *Proceedings of the Society of Photo-Optical Instrumentation Engineers*, San Jose, CA, 17–18 January; 10 pp. DOI. 10.1117/12.838903
- Castillo RP, James MR, Quinton JN, Taguas EV, Gómez JA. 2012. Comparing the accuracy of several field methods for measuring gully erosion. *Soil Science Society of America Journal* **July**: 1319–1332. DOI:10.2136/sssaj2011.0390.
- Chai T, Draxler RR. 2014. Root mean square error (RMSE) or mean absolute error (MAE)? – Arguments against avoiding RMSE in the literature. *Geoscientific Model Development Discussion* **7**: C473–C473.
- Chandler J. 1999. Effective application of automated digital photogrammetry for geomorphological research. *Earth Surface Processes and Landforms* **24**: 51–63.
- Chandler JH, Bryan P, Fryer JG. 2007. The development and application of a simple methodology for recording rock art using consumer-grade digital cameras. *The Photogrammetric Record* **22**(117): 10–21.
- Chandler J, Fryer J. 2013. AutoDesk 123D Catch—How accurate is it? *Geomatics World* : 28–30. January–February:
- Cramer M. 2004. Performance of medium format digital aerial sensor systems. *International Archives of Photogrammetry and Remote Sensing* **35**, part B5, *Proceedings of the 10th ISPRS Congress Technical Commission 5*, Istanbul, Turkey, 12–23 July; 769–774.
- Cooper MAR, Cross PA. 1988. Statistical concepts and their application in photogrammetry and surveying. *The Photogrammetric Record* **12**(71): 637–663.
- Diefenbach AK, Crider JG, Schilling SP, Dzurisin D. 2012. Rapid, low-cost photogrammetry to monitor volcanic eruptions—an example from Mount St. Helens, Washington, USA. *Bulletin of Volcanology* **74**(2): 579–587. DOI:10.1007/s00445-011-0548-y.
- Dietrich JT. 2016. Riverscape mapping with helicopter-based structure-from-motion photogrammetry. *Geomorphology* **252**: 144–157. DOI:10.1016/j.geomorph.2015.05.008.

- Eltner A, Kaiser A, Castillo C, Rock G, Neugirg F, Abellán A. 2016. Image-based surface reconstruction in geomorphology – merits, limits and developments. *Earth Surface Dynamics* **4**: 359–389. DOI:10.5194/esurf-4-359-2016.
- Federal Geographic Data Committee (FGDC). 1998. Geospatial positioning accuracy standards part 3—national standard for spatial data accuracy. National Spatial Data Infrastructure FDGC-STD-007.3-1998. FGDC: Reston, VA; 28 pp.
- Fonstad MA, Dietrich JT, Courville BC, Jensen JL, Carbonneau PE. 2013. Topographic structure from motion—a new development in photogrammetric measurement. *Earth Surface Processes and Landforms* **38**: 421–430. DOI:10.1002/esp.3366.
- Furukawa Y, Ponce J. 2010. Accurate, dense, and robust multiview stereo. *IEEE Transactions on Pattern Analysis and Machine Intelligence* **32**(8): 1362–1376. DOI:10.1109/TPAMI.2009.161.
- Gienko GA, Terry JP. 2014. Three-dimensional modeling of coastal boulders using multi-view image measurements. *Earth Surface Processes and Landforms* **39**(7): 853–864. DOI:10.1002/esp.3485.
- Glennie CL, Carter WE, Shrestha RL, Dietrich WE. 2013. Geodetic imaging with airborne LiDAR—the Earth's surface revealed. *Reports on Progress in Physics* **76**. DOI:10.1088/0034-4885/76/8/086801.24 pp
- Gomez C. 2014. Digital photogrammetry and GIS-based analysis of the bio-geomorphological evolution of Sakurajima Volcano, diachronic analysis from 1947 to 2006. *Journal of Volcanology and Geothermal Research* **280**: 1–13. DOI:10.1016/j.jvolgeores.2014.04.015.
- Gomez C, Hayakawa Y, Obanawa H. 2015. A study of Japanese landscapes using structure from motion derived DSMs and DEMs based on historical aerial photographs—new opportunities for vegetation monitoring and diachronic geomorphology. *Geomorphology* **242**: 11–20. DOI:10.1016/j.geomorph.2015.02.021.
- Gómez-Gutiérrez A, Schnabel S, Berenguer-Sempere F. 2014. Using 3D photo-reconstruction methods to estimate gully headcut erosion. *Catena* **120**: 91–101. DOI:10.1016/j.catena.2014.04.004.
- Greenwalt CR, Schultz ME. 1968. Principles of Error Theory and Cartographic Applications, US Air Force Aeronautical Chart and Information Center Technical Report No. 96. US Air Force Aeronautical Chart and Information Center: St Louis, MO; 98 pp.
- Gruen A. 2012. Development and status of image matching in photogrammetry. *The Photogrammetric Record* **27**(137): 36–57. DOI:10.1111/j.1477-9730.2011.00671.x.
- Guidi G, Gonizzi S, Micoli LL. 2014. Image pre-processing for optimizing automated photogrammetry performances. *Annals of the Photogrammetry, Remote Sensing and Spatial Information Sciences 11-5, ISPRS Technical Commission V Symposium*, Riva del Garda, 23–25 June; 145–152. DOI: 10.5194/isprsannals-11-5-145-2014
- Heritage G, Hetherington D. 2007. Towards a protocol for laser scanning in fluvial geomorphology. *Earth Surface Processes and Landforms* **32**: 66–74. DOI:10.1002/esp.1375.
- James MR, Quinton JN. 2014. Ultra-rapid topographic surveying for complex environments: the hand-held mobile laser scanner (HMLS). *Earth Surface Processes and Landforms* **39**(1): 138–142. DOI:10.1002/esp.3489.
- James MR, Applegarth LJ, Pinkerton H. 2012. Lava channel roofing, overflows, breaches, and switching—insights from the 2008–2009 eruption of Mt Etna. *Bulletin of Volcanology* **74**(1): 107–117. DOI:10.1007/s00445-011-0513-9.
- James MR, Robson S. 2012. Straightforward reconstruction of 3D surfaces and topography with a camera: accuracy and geoscience application. *Journal of Geophysical Research* **117**. DOI:10.1029/2011JF002289.17 pp
- James MR, Robson S. 2014. Sequential digital elevation models of active lava flows from ground-based stereo time-lapse imagery. *ISPRS Journal of Photogrammetry and Remote Sensing* **97**: 160–170. DOI:10.1016/j.isprsjprs.2014.08.011.
- Javernick L, Brasington J, Caruso B. 2014. Modeling the topography of shallow braided rivers using structure-from-motion photogrammetry. *Geomorphology* **213**: 166–182. DOI:10.1016/j.geomorph.2014.01.006.
- Lane SN, Westaway RM, Hicks DM. 2003. Estimation of erosion and deposition volumes in a large, gravel-bed, braided river using synoptic remote sensing. *Earth Surface Processes and Landforms* **28**(3): 249–271. DOI:10.1002/esp.483.
- Lipman PW, Mullineaux DR (eds). 1981. *The 1980 eruption of Mount St. Helens, Washington, US Geological Survey Professional Paper 1250*. US Geological Survey: Reston, VA; 844 pp.
- Li Z, Zhu Q, Gold C. 2005. *Digital Terrain Modeling: Principles and Methodology*. CRC Press: Boca Raton, FL; 323 pp.
- Lisein J, Linchant J, Lejeune P, Bouché P, Vermeulen C. 2013. Aerial surveys using an unmanned aerial system (UAS)—comparison of different methods for estimating the surface area of sampling strips. *Tropical Conservation Science* **6**(4): 506–520.
- Lowe DG. 2004. Distinctive image features from scale-invariant keypoints. *International Journal of Computer Vision* **60**(2): 91–110. DOI:10.1023/B:VISI.0000029664.99615.94.
- Mathews NA. 2008. *Aerial and Close-range Photogrammetric Technology—Providing Resource Documentation, Interpretation, and Preservation*, US Bureau of Land Management Technical Note 428. US Bureau of Land Management: Washington, DC; 42 pp.
- Mathews NA, Noble TA, Breithaupt B. 2006. The application of photogrammetry, remote sensing and geographic information system (GIS) to fossil resource management. In *Fossils from Federal Lands: New Mexico Museum of Natural History and Science Bulletin 34*, Lucas SG, Spielmann JA, Hester PM, Kenworthy JP, Santucci VL (eds). New Mexico Museum of Natural History and Science: Albuquerque, NM.
- Micheletti N, Chandler JH, Lane SN. 2015a. Investigating the geomorphological potential of freely available and accessible structure-from-motion photogrammetry using a smartphone. *Earth Surface Processes and Landforms* **40**(4): 473–486. DOI:10.1002/esp.3648.
- Micheletti N, Chandler JH, Lane SN. 2015b. Structure from Motion (SfM) Photogrammetry, Geomorphological Techniques, chapter 2, section 2.2. British Society of Geomorphology, London; 12 pp.
- Mosbrucker AR. 2010. Application of digital oblique photogrammetry for monitoring erosion and sedimentation at Mount St. Helens, Washington, USA. *Proceedings of the 4th Federal Interagency Hydrologic Modeling and 9th Federal Interagency Sedimentation Conference*, Las Vegas, NV, 27 June–1 July; 388.
- Mosbrucker AR. 2014. High-resolution DEM of Mount St. In *Helens Crater and Upper North Fork Toutle Basin, Washington, Based on Airborne LiDAR Survey of September 2009*. US Geological Survey Data Series. US Geological Survey: Reston, VA.
- Mosbrucker AR, Spicer KR, Christianson TS, Urich MA. 2015a. *Estimating Concentrations of Fine-grained and Total Suspended Sediment from Close-range Remote Sensing Imagery*, Technical Paper 61. SEDHYD: Reno, NV; 12 pp.
- Mosbrucker AR, Spicer KR, Major JJ, Saunders, DR, Christianson, TS, Kingsbury, CG. 2015b. Digital Database of Channel Cross-section Surveys, Mount St. Helens, Washington, US Geological Survey Data Series 951. US Geological Survey: Reston, VA; 9 pp. DOI: 10.3133/ds951
- Niethammer U, James MR, Rothmund S, Travelletti J, Joswig M. 2012. UAV-based remote sensing of the Super-Sauze landslide—evaluation and results. *Engineering Geology* **124**: 2–11. DOI:10.1016/j.enggeo.2011.03.012.
- Niethammer U, Rothmund S, James MR, Travelletti J, Joswig M. 2010. UAV-based Remote Sensing of Landslides, International Archives of Photogrammetry, Remote Sensing and Spatial Information Services XXXVIII, ISPRS Commission V. ISPRS: Newcastle-upon-Tyne; 496–501.
- Nouwakpo SK, Weltz MA, McGwire K. 2016. Assessing the performance of structure-from-motion photogrammetry and terrestrial LiDAR for reconstructing soil surface microtopography of naturally vegetated plots. *Earth Surface Processes and Landforms* **41**(3): 308–322. DOI:10.1002/esp.3787.
- Passalacqua P, Belmont P, Staley DM, Simley JD, Arrowsmith JR, Bode CA, Crosby C, DeLong SB, Glenn NF, Kelly SA, Lague D, Sangireddy H, Schaffrath K, Tarboton DG, Wasklewicz T, Wheaton JM. 2015. Analyzing high resolution topography for advancing the understanding of mass and energy transfer through landscapes—a review. *Earth Surface Reviews* **148**: 174–193. DOI:10.1016/j.earscirev.2015.05.012.
- Pitlick J, Meertens, CM, Major, JJ, Normandeau, J, Spicer K, Mosbrucker, AR, Mueller, E. 2010. Identifying sediment sources and quantifying rates of erosion along the North Fork Toutle River near Mount St. Helens, WA, Abstract G21A-0789. *Proceedings*,

- American Geophysical Union Fall Meeting*, San Francisco, CA, 13–17 December.
- Rippen DM, Pomfret A, King N. 2015. High resolution mapping of supra-glacial drainage pathways reveals link between micro-channel drainage density, surface roughness and surface reflectance. *Earth Surface Processes and Landforms* **40**(10): 1279–1290. DOI:10.1002/esp.3719.
- Rosnell T, Honkavaara E. 2012. Point cloud generation from aerial image data acquired by a quadcopter type micro unmanned aerial vehicle and a digital still camera. *Sensors* **12**(1): 453–480. DOI:10.3390/s120100453.
- Rydland PH Jr, Densmore BK. 2012. *Methods of Practice and Guidelines for Using Survey-grade Global Navigation Satellite Systems (GNSS) to Establish Vertical Datum in the United States Geological Survey*, US Geological Survey Techniques and Methods, Book 11, chapter D1. US Geological Survey: Reston, VA; 102 pp.
- Sanz-Ablanedo E, Chandler JH, Wackrow R. 2012. Parameterizing internal camera geometry with focusing distance. *The Photogrammetric Record* **27**(138): 210–226. DOI:10.1111/j.1477-9730.2012.00677.x.
- Shortis MR, Bellman CJ, Robson S, Johnston GJ, Johnson GW. 2006. Stability of zoom and fixed lenses used with digital SLR cameras. *Proceedings of the ISPRS Commission V Symposium of Image Engineering and Vision Metrology*, Dresden, 25–27 September; 285–290.
- Smith MW, Carrivick JL, Quincey DJ. 2016. Structure from motion photogrammetry in physical geography. *Progress in Physical Geography* **40**(2): 247–275. DOI:10.1177/0309133315615805.
- Smith MW, Vericat D. 2015. From experimental plots to experimental landscapes—topography, erosion and deposition in sub-humid badlands from structure-from-motion photogrammetry. *Earth Surface Processes and Landforms* **40**(12): 1656–1671. DOI:10.1002/esp.3747.
- Snaveley N, Seitz SM, Szeliski R. 2008. Modeling the world from internet photo collections. *International Journal of Computer Vision* **80**(12): 189–210. DOI:10.1007/s11263-007-0107-3.
- Staines KEH, Carrivick JL, Tweed FS, Evans AJ, Russell AJ, Jóhannesson T, Roberts M. 2015. A multi-dimensional analysis of pro-glacial landscape change at Sólheimajökull, southern Iceland. *Earth Surface Processes and Landforms* **40**(6): 809–822. DOI:10.1002/esp.3662.
- Sturznegger M, Stead D. 2009. Close-range terrestrial digital photogrammetry and terrestrial laser scanning for discontinuity characterization on rock cuts. *Engineering Geology* **106**: 163–182. DOI:10.1016/j.enggeo.2009.03.004.
- Thoeni K, Giacomini A, Murtagh R, Knies E. 2014. A comparison of multi-view 3D reconstruction of a rock wall using several cameras and a laser scanner. *Annals of the Photogrammetry, Remote Sensing and Spatial Information Sciences XL-5, ISPRS Technical Commission V Symposium*, Riva del Garda, 23–25 June; 573–580. DOI: 10.5194/isprsarchives-XL-5-573-2014
- Townsend JR. 2013. *The Development of a Geomatics-based Toolkit to Assess the Impact of Engineered Grade Building Structures on the North Fork Toutle River, Mt. St. Helens*, MSc Thesis. University of Nottingham; 158 pp.
- Ullman S. 1979. The interpretation of structure from motion. *Proceedings of the Royal Society of London. Series B* **203**(1153): 405–426. DOI:10.1098/rspb.1979.0006.
- Wackrow R, Chandler JH. 2008. A convergent image configuration for DEM extraction that minimizes the systematic effects caused by an inaccurate lens model. *The Photogrammetric Record* **23**(121): 6–18. DOI:10.1111/j.1477-9730.2008.00467.x.
- Wackrow R, Chandler JH. 2011. Minimizing systematic error surfaces in digital elevation models using oblique convergent imagery. *The Photogrammetric Record* **26**(133): 16–31. DOI:10.1111/j.1477-9730.2011.00623.x.
- Walker AS, Petrie G. 1996. Digital photogrammetric workstations 1992–96. *International Archives of Photogrammetry and Remote Sensing 31, Part B2, Proceedings of the 18th ISPRS Congress Technical Commission 2*, Vienna, 9–19 July; 384–395.
- Welty EZ, Bartholomaeus TC, O'Neil S, Pfeffer WT. 2013. Cameras as clocks. *Journal of Glaciology* **59**(214): 275–286. DOI:10.3189/2013JG12J126.
- Westaway RM, Lane SN, Hicks DM. 2003. Remote survey of large-scale braided, gravel-bed rivers using digital photogrammetry and image analysis. *International Journal of Remote Sensing* **24**(4): 795–815. DOI:10.1080/01431160110113070.
- Westoby MJ, Brasington J, Glasser NF, Hambrey MJ, Reynolds JM. 2012. 'Structure-from-Motion' photogrammetry: a low-cost, effective tool for geoscience applications. *Geomorphology* **179**: 300–314. DOI:10.1016/j.geomorph.2012.08.021.
- Wheaton JM, Brasington J, Darby SE, Sear DA. 2010. Accounting for uncertainty in DEMs from repeat topographic surveys: improved sediment budgets. *Earth Surface Processes and Landforms* **35**(2): 136–156. DOI:10.1002/esp.1886.
- Willmott CJ, Matsuura K. 2005. Advantages of the mean absolute error (MAE) over the root mean square error (RMSE) in assessing average model performance. *Climate Research* **30**: 79–82. DOI:10.3354/cr030079.
- Woodget AS, Carbonneau PE, Visser F, Maddock I. 2015. Quantifying submerged fluvial topography using hyperspatial resolution UAS imagery and structure from motion photogrammetry. *Earth Surface Processes and Landforms* **40**(1): 47–64. DOI:10.1002/esp.3613.
- Wu C. 2007. SiftGPU: A GPU Implementation of Scale Invariant Feature Transform (SIFT). University of North Carolina. <http://cs.unc.edu/~ccwu/siftgpu/> [December 2013].
- Wu C. 2013. Towards linear-time incremental structure from motion. *Proceedings, Joint 3DIM/3DPVT Conference (3DV)/University of Washington*. <http://ccwu.me/vsfm/vsfm.pdf> [December 2013].
- Wu C, Agarwal S, Curless B, Seitz SM. 2011. Multicore bundle adjustment. *Proceedings, 24th Conference on Computer Vision and Pattern Recognition (CVPR)/University of Washington*. <http://grail.cs.washington.edu/projects/mcbs/pba.pdf> [December 2013].